Final Technical Report for DOE Grant Number DE-SC0002508

Title: SISGR - Isotopic Studies of O-O Bond Formation During Water Oxidation

Reporting Period: 9/14/2009-12/14/14

Applicant/Principal Investigator: Dr. Justine P. Roth

PI's Institutional Address: Dept. of Chemistry, Johns Hopkins University, 3400 N. Charles St., Baltimore, MD 21218

PI's Contact Information: Phone: (410) 516-7835, Email: jproth@jhu.edu

Publication Date: 3/3/2015

II. Project Objectives:

Research during the proposed project period will focus on the mechanisms of water oxidation catalysis by transition metal species in aqueous environments. New directions involving naturally occurring extended transition metal oxides, resembling the oxygen-evolving complex in photosystem II,[1] will be pursued. The objectives below will provide insights needed to develop viable catalysts[2] for producing electricity and solar fuels that can serve the world's energy needs while transforming the environment and global economy.[3]

$$2H_2O + \text{sunlight} \xrightarrow[\text{catalyst}]{} O_2 + 4H^+ + 4e^-$$

Objective 1.

Driving-Force Dependence of Kinetics and Oxygen Kinetic Isotope Effects (^{18}O KIEs).
Bulk electrolysis will be used to generate O_2 from water oxidation catalyzed by structurally defined transition metal complexes. Analysis of the O_2 will allow probing of ^{18}O KIEs at controlled electrolytic potentials to examine the effect of varying thermodynamic driving-force. Complementary kinetic studies of water oxidation in H_2O and D_2O will expose the intrinsic barrier, revealing contributions from solvent reorganization and/or proton transfer. Mechanisms of O−O bond formation will be proposed based on the results and then evaluated by comparing measured ^{18}O KIEs to those calculated using Density Functional Theory (DFT).[4]

Objective 2.

Probing Catalytic Intermediates Capable of Reversible O−O Bond Formation.
Computational investigations of water oxidation have frequently assumed that the O−O bond forms reversibly during catalysis.[5] Yet recent measurements of large normal ^{18}O KIEs, together with solvent deuterium isotope effects, have implicated irreversible O−O bond formation by water attack mechanisms. To reconcile these proposals, metal hydroperoxo intermediates will be generated from H_2O_2 in ^{18}O-enriched water and examined, using isotope ratio mass spectrometry (IRMS), to detect reversible fragmentation to a metal oxo species and H_2O.[6]

Objective 3.

Mechanistic Characterization of Photocatalysis by Insoluble Transition Metal Oxides.
Competitive ^{18}O KIEs will be determined on reactions of a structurally defined transition metal oxide photo-catalyst. Tungsten trioxide (WO_3) is a semiconductor characterized in various crystalline as well as amorphous states and shown to catalyze water oxidation,[7] with reasonably

high quantum yields, producing O_2 over the course of several hours. Experimental studies coupled with DFT calculations could provide first-of-a-kind mechanistic insights into how O−O bonds form at surfaces of robust inorganic materials, increasingly used to fabricate photo-electrodes and produce solar hydrogen.

III. Results from Previous Funding Period

We examined a number of reactions where O−O bond making is rate-determining,[8,9] using an oxygen isotope fractionation technique which employs *natural abundance* water and isotope ratio mass spectrometry (IRMS).[4,8,9] Computational methods have also been developed to test mechanistic interpretations. Several homogeneous systems derived from manganese, iron, ruthenium and iridium complexes have been explored and preliminary results obtained on surface reactions of tungsten trioxide (WO_3).

A. Experimental and Computational Procedures:

Oxygen isotope fractionation applied to the determination of competitive oxygen kinetic isotope effects (^{18}O KIEs) reflects the rates of $^{16,16}O_2$ and $^{16,18}O_2$ produced from the oxidation of natural abundance water.[4,10] In addition, tracer experiments with ^{18}O-labeled water have been used to detect reversible O−O bond making and breaking, which gives rise of oxygen equilibrium isotope effects (^{18}O EIEs). We have found specific Density Functional Theory (DFT) calculations that are ideally suited for the quantum mechanical calculation of heavy atom isotope effects within the harmonic oscillator approximation.

Changing $^{18}O/^{16}O$ ratios analyzed IRMS by reflect enrichment or depletion of the light isotope in the O_2 formed, relative to the water from which it was produced, leading to normal (>1) or inverse (<1) ^{18}O KIEs, respectively. The size and sign of the isotope effects arise from compensating enthalpic and entropic factors. We have used DFT to model such behavior for reversible reactions of O_2 with transition metals and reproduced temperature-dependent trends in experimental ^{18}O EIEs.[9b] In addition, we have measured and predicted ranges of ^{18}O KIEs on O–O bond forming reactions referred to in Scheme 1 as oxo-coupling and water attack.[4]

Scheme 1. Oxygen Isotope Effects on intramolecular and intermolecular reactions.

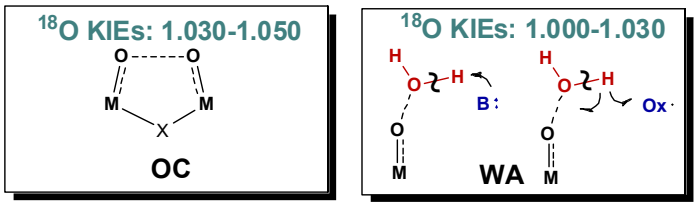

An apparatus akin to that shown in Figure 1 was originally constructed for measurement of the ^{18}O content of O_2 formed by photosynthetic water oxidation by whole cells and cell fractions (*vide infra*).[10] The processes used to isolate and purify O_2 from other condensable gases as well as to carry out the quantitative combustion of O_2 to CO_2, measure gas pressures and prepare samples *in vacuo* have also been described, along with the derivation of competitive ^{18}O KIEs.[9] Importantly, errors are typically an order of magnitude smaller than the measured

^{18}O KIEs, potentially allowing mechanisms of **OC** and **WA** to be distinguished experimentally. The high precision owes to the competitive methodology for determining $^{18}O/^{16}O$ ratios, the use of natural abundance chemicals, which do not exhibit contamination, and dual-inlet isotope ratio mass spectrometers that allow ratios to be determined to $\pm$ 0.0002. The apparatus in Figure 1 can be modified, as described in the following proposal, to allow ^{18}O KIE measurements on photo-catalytic and electro-catalytic reactions.

Figure 1. Apparatus for competitive oxygen-18 kinetic isotope effect measurements.[9c]

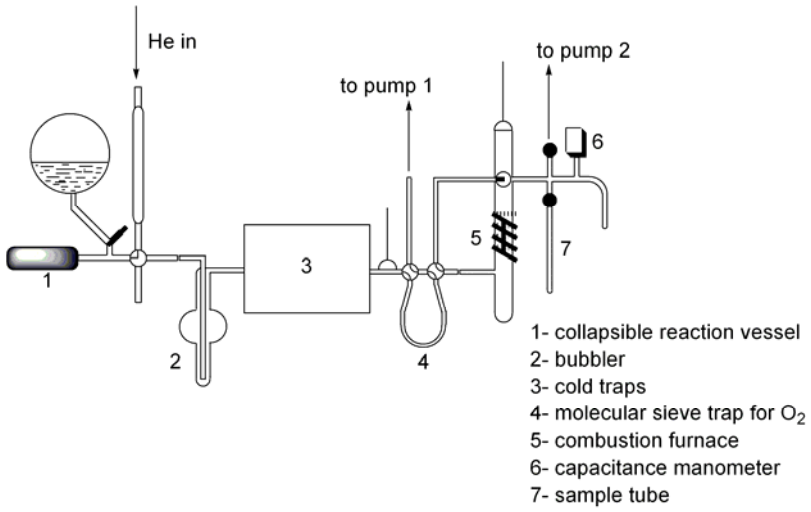

From the beginning, our efforts have stressed the complementary use of experiments and calculations. Initially, we verified the use of a particular DFT protocol to optimize structures and obtain vibrational frequencies needed to predict ^{18}O EIEs as the product of reduced partition function ratios corresponding to isotopic zero point energy (*ZPE*), vibrational excitation energy (*EXC*) and the mass and moments of inertia (*MMI*) in Eq 1.[9a,9b,11]

$$^{18}\text{O EIE} = ZPE \times EXC \times MMI \quad (1)$$

Results of the studies described here reveal that ^{18}O KIEs can also be predicted using Transition State Theory formalism. Specifically, Eq 2 defines the ratio of rate constants, corresponding to reactions of the light ($^{16}O-^{16}O$) and heavier ($^{16}O-^{18}O$) oxygen isotopologues. Terms include the pseudo-equilibrium constant for attaining the transition state from the reactant state, $^{18}K_{TS}$, which is equivalent to isotopic *ZPE* × *EXC* × *VP*, where the vibrational product is the *MMI* minus the mode that defines the reaction coordinate. This contribution, $^{18}v_{RC}$, is the ratio of mass-dependent imaginary frequencies.

(2) $$^{18}\text{O KIE} = {}^{18}\nu_{RC} \times {}^{18}K_{TS}$$

The $^{18}\nu_{RC}$ is invariably ≥ 1 due to its definition as the ratio of frequencies for light to heavy isotopologues. The $^{18}K_{TS}$ term can be normal or inverse depending on the enthalpy and entropy changes that characterize the reaction. In all cases examined thus far, small to inverse ^{18}O EIEs have been calculated for O−O bond forming reactions of metal oxo species. Yet normal ^{18}O KIEs resulting from $^{18}\nu_{RC}$ terms that dominate the $^{18}K_{TS}$ terms are calculated (and observed) for the same reactions.[4,12]

B. Water Oxidation by Ferrate:

Large normal ^{18}O KIEs ≥1.03 were first observed on water oxidation by potassium ferrate ($K_2Fe^{VI}O_4$). An electrochemical driving force of $\Delta E°$ = 0.97 V is calculated for the net reaction in Eq 3 based on the half-cell potentials: $\mathbf{Fe^{VI}O_4^{2-} + 8H^+ + 3e^- \rightarrow Fe^{III} + 4H_2O}$ ($E°$ = 2.2 V vs. NHE) and $\mathbf{O_2 + 4H^+ + 4e^- \rightarrow 2H_2O}$ ($E°$ = 1.23 V vs. NHE). Due to its instability in the presence of protons, the chemical mechanism of ferrate-mediated water oxidation has received relatively limited attention.[13]

The high-valent, oxyanion has been shown to undergo rapidly exchange with H_2O[13a] and exist in a triplet ground state.[4] DFT calculations described below suggest that the asymmetric build-up of alpha spin occurs upon protonation. Thus, it was anticipated that the low pH form of ferrate $[H_3FeO_4]^+$ could rapidly undergo dimerization and condensation, forming a μ-oxo bridged di-iron(VI) complex structurally resembling dichromic acid and pyrophosphoric acid. The proposed $[H_4Fe_2O_7]^{2+}$ has since been demonstrated kinetically competent for water oxidation, consistent with the complex reaction stoichiometry of Eq 3.

(3) $$\mathbf{4[H_3Fe^{VI}O_4]^+ + 8H_3O^+ \rightarrow 4Fe^{3+} + 3O_2 + 18H_2O}.$$

Acidified ferrate solutions rapidly generate molecular oxygen with a 4:3 stoichiometry.[4,13] Data collected at pH 1.0 in Figure 2 reveal the oxygen isotope fractionation of O_2 produced from natural abundance H_2O as well as the optical changes on the timescale of seconds upon adding $HClO_4$ to FeO_4^{2-}. Rapid-mixing stopped flow electronic absorption was used to test for the intermediacy of μ-1,2-oxo-bridged diferrate, $[H_4Fe^{VI}_2O_7]^{2+}$, prior to oxidizing water to O_2 and forming iron(III) as the final product(s).

Figure 2. (a) Isotope fractionation derived from the analysis of O_2 upon K_2FeO_4-mediated water oxidation. (b) The corresponding optical changes upon acidification.

(a)

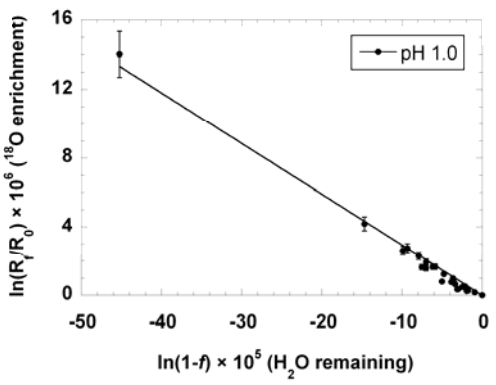

(b)

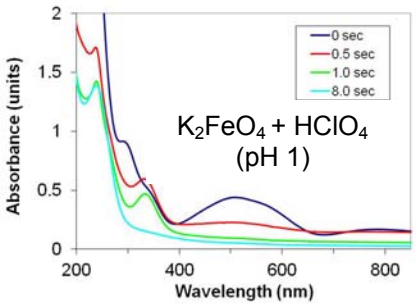

The pH-jump stopped-flow experiments in Figure 3 are consistent with formation of a di-ferrate intermediate. The kinetics in the visible region reveals a bimolecular reaction of ferrate at pH 2.7 and a unimolecular reaction at pH 1.0, where di-ferrate forms rapidly on the experimental timescale. These observations are consistent with the calculated spectra at pH 2.7 and pH 1.0. The $[H_3FeO_4]^+$ condenses and dimerizes to produce water and $[H_4Fe_2O_7]^{2+}$. The initial spectrum at pH 1.0 corresponds to the condensation product, labeled B, which decays to form C and O_2 in the final spectrum.

Figure 3. Electronic absorption changes collected using an OLIS RSM1000 rapid-scanning spectrophotometer. Time traces at pH 2.7 corresponding to dimerization and condensation (top) and at pH 1.0 where changes coincide with O−O bond formation and O_2 evolution (bottom).

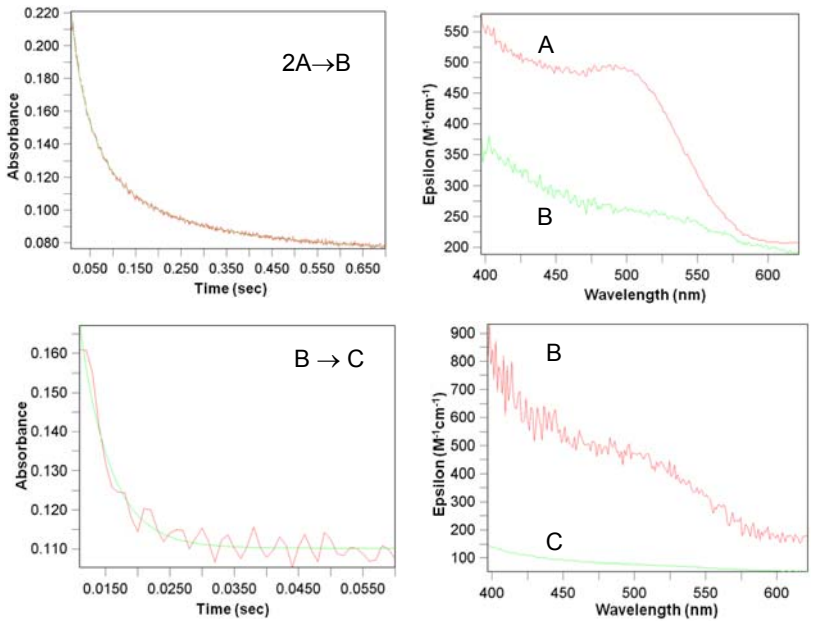

Species C is likely an unstable di-iron(IV) species that undergoes disproportionation by oxo-transfer. This reaction, which would produce di-iron(II) and re-form the reactive di-iron(VI) species, is thermodynamically favored with respect to formation of di-iron(III) and a high-energy di-iron(V) intermediate.[17,18] As a result, iron(II) complexes are expected to comproportionate with iron(IV) complexes to form iron(III) as the final products upon acidification of ferrate followed by mix-freeze EPR analysis on a timescale >10 seconds.[4]

Corroboration of the proposed mechanism in Figure 4 comes from the pH and pD profiles in H_2O and D_2O, which reveal *inverse* solvent isotope effects on the bimolecular rate constants of ferrate between pH/pD 1.3 and 2.7. The inverse effect disappears with increasing acidity and a solvent isotope effect indistinguishable from unity is observed at pH/pD 1.0, where the reaction

appears unimolecular. The second order rate constants are fitted to a one-state model with a pK_a of ~1.5, in excellent agreement with an earlier assignment to $[H_3FeO_4]^+$.[17,18] There is an isotope shift of the pK_a to ~1.9 for $[D_3FeO_4]^+$ as expected in D_2O.[4]

Figure 4. Proposed mechanism and kinetic profile of the bimolecular rate constant (k_{bi}) for di-ferrate formation versus solution acidity in H_2O (red circles) and D_2O (blue squares). Data are fitted to the expression: log k_{obs} = log[k_{max}/(1+10^{pH-pKa})], where k_{max} = 2.5 × 10^5 $M^{-1}s^{-1}$ and pK_a = 1.5 (in H_2O) or 1.9 (in D_2O).

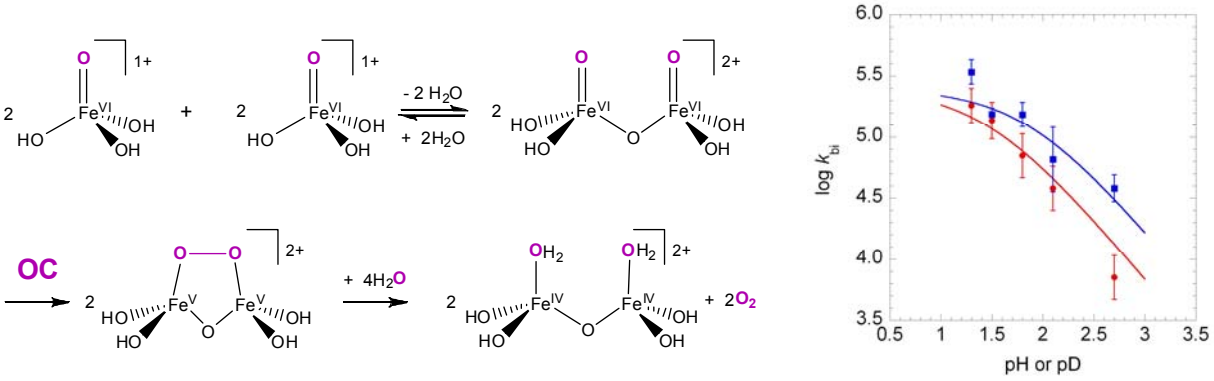

C. Computational Studies of O−O Bond Formation:

A second objective of these studies was to compare measured ^{18}O KIEs to computational predictions. DFT optimized geometries were obtained using a previously calibrated[14,15] *m*PW[16] functional. The calculations on ferrate did not include the small energy corrections for spin contamintaion.[4] Rather, ferrate was formulated as a ground state triplet and diferrate was assumed to be in unrestricted singlet state due to strong antiferromagnetic coupling through the μ-oxo bridge. ^{18}O KIEs were computed from gas phase structures in all protonation states. Stationary points were verified by intrinsic reaction coordinate (IRC) calculations.[17] Vibrational frequency analysis within the harmonic oscillator approximation provided the 3N-6 vibrations for the precursor and 3N-7 vibrations for the transition state (TS, ‡), where N is the total number of atoms. These vibrations were used in the reduced partition function ratios described above to solve the ^{18}O KIE according to Eq 2. Many transition states were considered for the monomeric and dimeric forms of ferrate as well as the **OC** and **WA** mechanisms in Scheme 2.[4]

Scheme 2. Potential water attack (**WA**) and oxo-coupling (**OC**) mechanisms of diferrate.

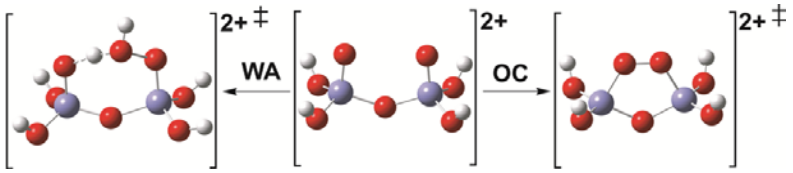

The experimental ^{18}O KIE of 1.0303 ± 0.0014 on the formation of O_2 from di-ferrate at pH 1.0 was reproduced to a remarkable level of agreement using DFT-derived vibrations of the

precursor and transition state.[4] The experimental and computational results favored the presence of **OC** via $[H_4Fe^{VI}_2O_7]^{2+}$. In fact, in all protonation states oxo-coupling (**OC**) was uniformly favored over water attack (**WA**) in this geometrically constrained system. The free energy barriers for **OC** were between 8 and 25 kcal mol^{-1} lower than those associated with **WA** and the calculated barriers decreased with the increased protonation level. Transition states for various monomeric ferrates were also investigated and found to exhibit prohibitively high energy barriers and ^{18}O KIEs outside the experimental range.[4] ^{18}O KIEs of 1.0308 and 1.0302 were predicted for **OC** reactions of $[H_4Fe_2O_7]^{2+}$ and $[H_3Fe_2O_7]^{+}$. Significantly smaller ^{18}O KIEs, from 1.004 to 1.0147, were calculated for the alternative **WA** mechanisms. As mentioned above, the barrier to **OC** (4.27 kcal mol^{-1}) is significantly smaller than the barrier to **WA** (12.40 kcal mol^{-1}) for $[H_4Fe_2O_7]^{2+}$. The same holds true for $[H_3Fe_2O_7]^{+}$ where **OC** (6.22 kcal mol^{-1}) has a barrier well below that associated with **WA** (from 20.73 to 22.74 kcal mol^{-1}), where two transition states are possible due to asymmetry in the structure.

The experimental and computational study of ferrate/diferrate reactivity provides benchmark ^{18}O KIEs for various modes of O−O bond formation by synthetic and natural water oxidation catalysts. The electronic structure of the reactive ferryl (Fe^{VI}=O) actually resembles the "dangling" manganyl (Mn^{V}=O or Mn^{IV}–O•) proposed in the OEC of PSII.[1] Yet under catalytic conditions, the OEC reacts with a rather small inverse apparent ^{18}O KIE approaching unity. This observation seems more consistent with O_2 release from a Mn−O_2 adduct. Though such a species has been proposed at high O_2 pressures, its authenticity has been questioned.[18,19] Alternative explanations for the slightly inverse ^{18}O KIE reported by several researchers has been discussed in terms of obscuring effects of O_2 production competing with O_2 consumption in various PSII preparations.[10,20]

D. Water Oxidation by Ruthenium Catalysts:

Related monomeric and dimeric ruthenium complexes have been the subject of numerous mechanistic investigations.[21,22,23] For this reason, we chose to conduct experiments on the complexes in Figure 5: $[Ru^{II}(bpy)(tpy)(OH_2)](ClO_4)_2$ (**Ru**), $[Ru^{II,II}(tpy)_2(OH_2)_2(\mu\text{-Hbpp})](ClO_4)_2$ (**Ru_2^{Hbpp}**, Hbpp = bis(2-pyridyl)-3,5-pyrazolate) and *cis,cis*-$[Ru^{III}(bpy)_2(OH_2)(\mu\text{-O})]_2](ClO_4)_4$ (**Ru_2^{BD}**). ^{18}O KIEs were determined under conditions previously used for isotope labeling studies, where mechanisms are inferred from the O_2 formed upon stoichiometric oxidation.

Figure 5: The ruthenium complexes examined and abbreviations used.

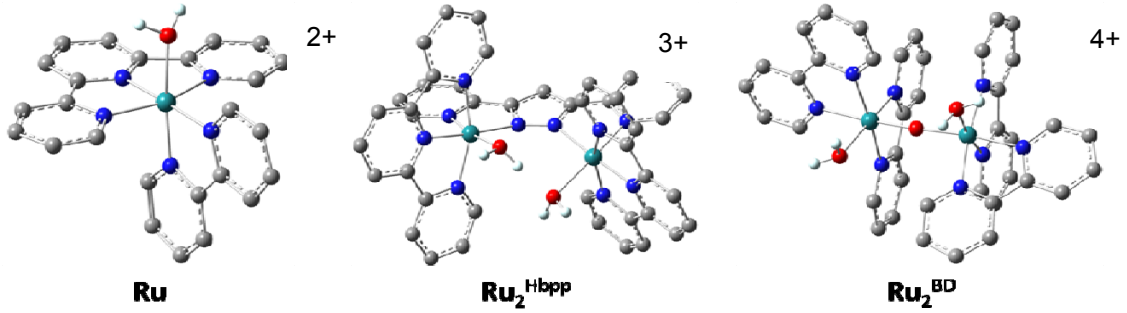

E. Kinetics of Catalysis:

Initial rates of catalytic water oxidation were determined using a Clark-type O_2 electrode (YSI) at 22.0 ± 0.2 °C. Ceric ammonium nitrate, $(NH_4)_2Ce^{IV}(NO_3)_6$, referred to throughout as CAN, served as the sacrificial oxidant in perchloric acid or triflic acid solutions. Ionic strength in H_2O and D_2O (μ = 1.0 M) was maintained by addition of sodium triflate or lithium perchlorate. Reactions were initiated by introducing 1-10μL of the ruthenium complex or CAN into a 1mL stirring solution saturated with air.

CAN-dependent and independent rates were determined from data fitted to the expression: rate/[Ru complex] = $k_{cat}[CAN]^n/(K_{CAN}^n + [CAN]^n)$ in Figure 6. The coefficient n = 1 for $\mathbf{Ru_2^{Hbpp}}$ and $\mathbf{Ru_2^{BD}}$ where normal hyperbolic (Michaelis-Menten-like) behavior is observed. The coefficient n = 3 for **Ru** where a sigmoid behavior is present, consistent with an induction phase. Although it is difficult to envision the coordination of Ce^{IV} to **Ru** derived species, the same behavior would be anticipated for multimerization of CAN-derived species, which could exert a positive effect upon catalysis by increasing the rate of oxidizing **Ru** to the reactive precursor that undergoes O−O bond formation in the CAN-independent region.

Figure 6: Water oxidation initiated by **Ru** (a), $\mathbf{Ru_2^{BD}}$ (b) and $\mathbf{Ru_2^{Hbpp}}$ in 0.1 M $HClO_4$ (c) or 0.1 M HOTf (d). Experiments at saturating CAN are compared in H_2O (circles) and D_2O (squares).

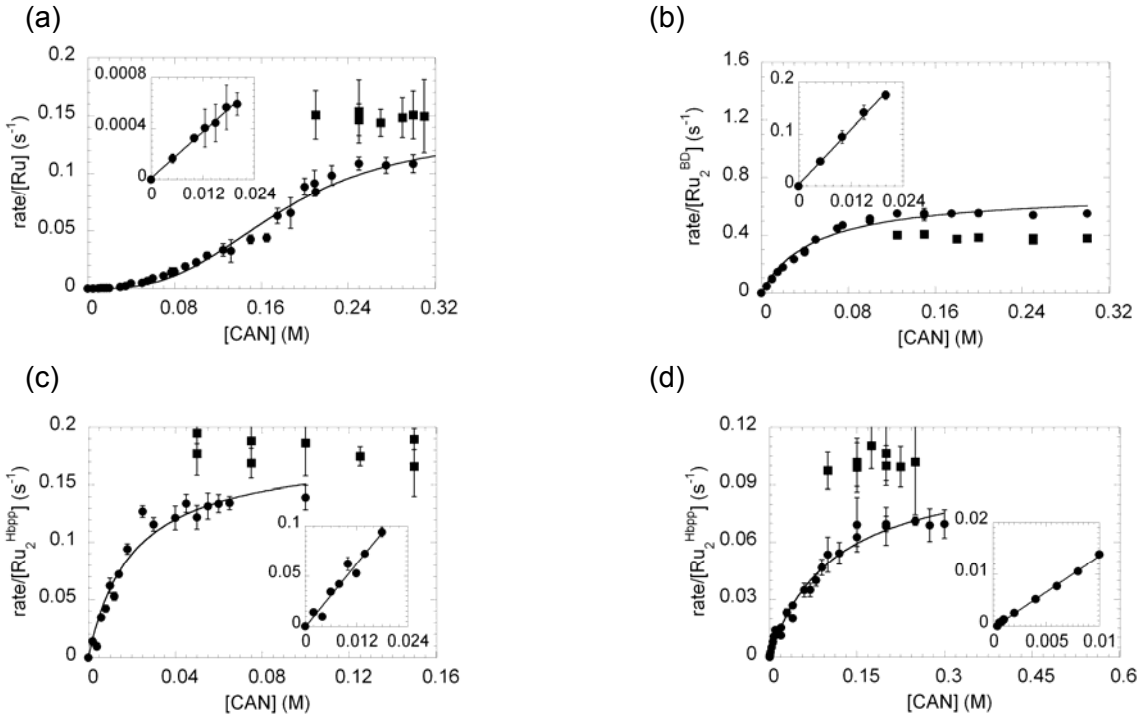

Solvent deuterium isotope effects on k_{cat} were determined for each of the catalytic reactions. A small inverse solvent deuterium isotope effect of 0.92 ± 0.08 was observed for **Ru**, whereas

an effect indistinguishable from unity was observed for $\mathbf{Ru_2^{Hbpp}}$ in different acidic media. Under these conditions, $\mathbf{Ru_2^{BD}}$ exhibited a normal solvent deuterium isotope effect of 1.85 ± 0.16. It is noteworthy that the relatively small solvent isotope effects could arise from pre-equilibrium proton transfer in competition with a normal primary kinetic isotope effect due to transfer of a solvent-exchangeable hydrogen in the turnover-limiting step.[24]

Table 1. Steady-state kinetic parameters in 0.1 M $HClO_4$ and 22.0 ± 0.2°C unless noted. [a]

Initiator	k_{cat}/K_{CAN} ($M^{-1}s^{-1}$)	k_{cat} (s^{-1})	$^{D2O}k_{cat}$ [b] (s^{-1})	$\Delta G^{\ddagger}_{unimolecular}$ (kcal mol^{-1})
Ru	0.0301 ± 0.0024 [c]	0.136 ± 0.011	0.148 ± 0.008	18.7 ± 1.4
$\mathbf{Ru_2^{BD}}$	8.87 ± 0.64	0.704 ± 0.054	0.380 ± 0.032	17.8 ± 1.4
$\mathbf{Ru_2^{Hbpp}}$	5.20 ± 0.84	0.181 ± 0.024	0.184 ± 0.020	18.6 ± 2.5
$\mathbf{Ru_2^{Hbpp}}$ [d]	1.38 ± 0.44	0.103 ± 0.011	0.102 ± 0.004	18.9 ± 2.0

[a] At pH or pD 1.0 and μ = 1.0 M. [b] In D_2O. [c] Attenuating the data set to the exponential phase gives 0.38 M^{-2} s^{-1}. See reference 12a for details. [d] Measured in 0.1 M protiated or deuterated triflic acid.

F. Competitive Oxygen Kinetic Isotope Effects:

^{18}O KIEs were determined using the apparatus and methodology described above and in a study that focused on **Ru**.[12] Solutions were saturated with He prior to initiation by addition of the oxidant. Most experiments employed CAN in $HClO_4$ at pH 0.0 and 1.0 and some involved $[Ru^{III}(bpy)_3]^{3+}$ photo-generated in 0.05 M potassium phosphate buffer (KP_i) at pH 7.2. The latter employed hundred micromolar to millimolar quantities of $[Ru^{II}(bpy)_3](Cl)_2$ and potassium persulfate ($K_2S_2O_8$) using exhaustive photolysis as previously described.[12] O_2 samples were routinely isolated and purified from condensable gases, such as CO_2, N_2O, NO and NO_2, by passage of the sample through a series of cold traps. Upon complete combustion[25] of the O_2 produced exclusively by catalytic water oxidation, CO_2 samples of identical pressure and $^{18}O/^{16}O$ were analyzed by IRMS at facilities at Johns Hopkins and the University of Waterloo. The low conversion of the water to O_2 allows the ^{18}O KIE to be estimated from the $^{18}O/^{16}O$ of the source H_2O (R_0) relative to the $^{18}O/^{16}O$ in the O_2 produced (R_p), *i.e.*, R_0/R_p.[4,12] The more precise relationship given in Eq 4 also considers the fractional yield (f) of O_2. The $^{18}O/^{16}O$ at a specific conversion (R_f) is thus defined by the mass-balance relationship: $R_0 = R_f(1\text{-}f) + R_p(f)$. The isotopic composition of unreacted H_2O, R_0 = 0.9940 ± 0.0008 vs. Vienna Standard Mean Ocean Water was confirmed by repeated measurements. The ^{18}O KIEs derived from the data in Figure 7 are quoted with one standard deviation errors. Calculation of the ^{18}O KIE from R_0/R_p gave indistinguishable results although the errors were significantly larger.

$$^{18}\mathrm{O\,KIE} = \left[1 + \frac{\ln\left(R_f/R_0\right)}{\ln\left(1-f\right)}\right]^{-1} \cong R_0/R_P$$

(4)

Figure 7. Data used to derive ^{18}O KIEs on water oxidation catalysis initiated by **Ru** (red squares), $\mathbf{Ru_2^{BD}}$ (green circles) and $\mathbf{Ru_2^{Hbpp}}$ (blue diamonds) in 0.1 M $HClO_4$ solutions of CAN (0.01-0.55 M). Inset: ^{18}O KIE versus catalyst turnover number (TON).

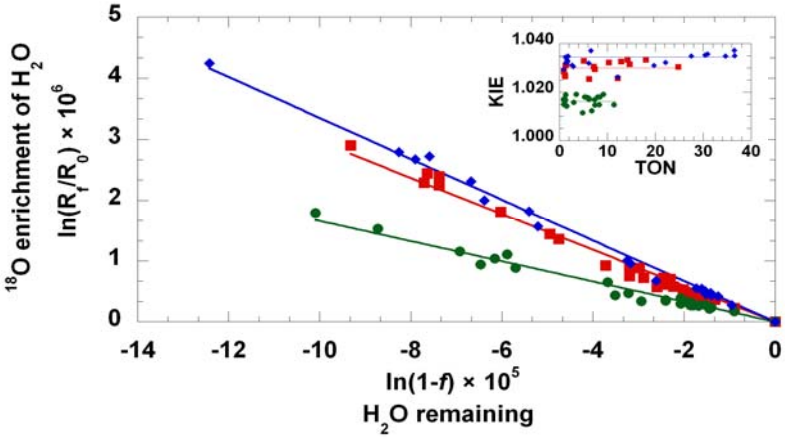

The data in Figure 7 show ^{18}O enrichment of the H_2O remaining in solution and therefore normal ^{18}O KIEs on the formation of O_2. Values are independent of turnover number (TON) and vary significantly from 1.0169 for $\mathbf{Ru_2^{BD}}$ up to 1.0306 for **Ru** and 1.0347 for $\mathbf{Ru_2^{Hbpp}}$. Under neutral conditions and using a weaker one-electron oxidant, the ^{18}O KIEs are two to three times smaller. Values of 1.0055 ± 0.0028 for $\mathbf{Ru_2^{BD}}$ and 1.0141 ± 0.0008 for **Ru** result from different transition states, possibly involving phosphate as the proton acceptor. A change in the rate-limiting step could also result from the use of the ca. 0.3 V weaker oxidant. Comparison to $\mathbf{Ru_2^{Hbpp}}$ was not possible because of its lack of photocatalytic activity.

^{18}O KIEs on water oxidation are complex measurements that potentially reflect a number of reaction steps, beginning with the coordination of H_2O ($^{18}K_{H2O}$ or $^{18}k_{H2O}$),[26] including oxidative steps ($^{18}K_{ox}$ or $^{18}k_{ox}$),[14,27,28] O−O bond formation ($^{18}k_{OO}$), and O_2 extrusion.[29] The equations below represent definitions of the ^{18}O KIEs in the fully reversible and irreversible limits of behavior. The ^{18}O KIE in Eq 5 is determined by a series of reversible steps preceding rate-limiting O−O bond formation. Yet in Eq 6, all steps are treated as kinetically irreversible making the ^{18}O KIE a weighted average dominated by the step with the highest energy transition state. O_2 release steps are not included in either expression because they lead to inverse ^{18}O KIEs, approaching unity,[29c] in contrast the ^{18}O KIEs observed.

(5) $$^{18}\text{O KIE} = \left(^{18}K_{\text{H2O}}\right) \times \left(^{18}K_{\text{ox}}\right)_{(n=1-4)} \times {}^{18}k_{\text{OO}}$$

$$(6) \quad {}^{18}\mathrm{O\,KIE} = \frac{w_1\,{}^{18}k_{\mathrm{H2O}} + w_2\,{}^{18}k_{\mathrm{ox}} + w_3\,{}^{18}k_{\mathrm{ox}} + w_4\,{}^{18}k_{\mathrm{ox}} + w_5\,{}^{18}k_{\mathrm{ox}} + w_6\,{}^{18}k_{\mathrm{OO}}}{w_1 + w_2 + w_3 + w_4 + w_5 + w_6}$$

Table 2. Summary of ^{18}O KIEs on catalytic water oxidation at 22 ± 2 ºC.

Initiator	**^{18}O KIE$_{measured}$ (pH 1.0)** [b]	**Proposed Transition State** [b]	**^{18}O KIE$_{calculated}$** *m*PW / M06-L
Ru	1.0306 ± 0.0004	**WA**[4a]	1.0240 / 1.0303
Ru_2^{BD}	1.0169 ± 0.0003	**WA**[2]	1.0151 / 1.0172
Ru_2^{Hbpp}	1.0347 ± 0.0004	**OC**	1.0311 / 1.0447

[a] 0.1 M $HClO_4$ (pH 1.0) with CAN (0.01-0.55 M). [b] The superscript designates the number and configuration of explicit water molecules (see Figures 8-10).

G. Computational Analyses:

All geometries were fully-optimized at two levels of DFT.[30] One approach employed the mPW functional[31] previously validated,[4,6,9a,9b,14] the LANL2DZ pseudopotential basis set for Ru,[32] 6-311G(d) basis set for O and N, and 6-31G basis set for C and H.[33] The second approach employed the M06-L functional,[34] along with the Stuttgart [8s7p6d2f | 6s5p3d2f] ECP28MWB contracted pseudo-potential basis set[35] for Ru and 6-31G(d) basis[36] for all other atoms. Stationary points were verified by the analytic computation of vibrational frequencies and intrinsic reaction coordinate (IRC) calculations.[37]

Bulk solvation effects on the free energy barriers to O−O bond formation were included using the SMD model[38] or by applying single point corrections.[14] Structures in the water oxidation mechanisms investigated have electronic structures that are not well-described by a single determinant so that the standard Kohn-Sham DFT is not directly applicable for the accurate prediction of spin states.[39] In such instances, the Yamaguchi broken-spin-symmetry (BS) procedure was used to compute energies of "spin-purified" lowest spin state.[40] This broken-symmetry DFT approach has proven effective for predicting state-energy splittings in transition metal complexes.[41]

H. Calculations of ^{18}O KIEs:

Calculations were performed using the Transition State Theory formalism described in the opening section. Once the transition state (TS) for a reaction was identified using the DFT methods above, the normal and imaginary vibrational frequencies of the ^{16}O−^{16}O and ^{16}O−^{18}O-conaining isotopologues were analyzed. No scaling or correction for anharmonicity was applied and isotopic vibrational data were used to compute ^{18}O KIEs according to Eq 2.

The accurate calculation of ^{18}O KIEs relies on the ability of DFT to predict structures and the mass-dependence of stable and imaginary vibrational modes. The individual frequencies need not be computed with great accuracy. Rather, the net isotope shift of vibrations dictates the isotope effect. A related approach has been used extensively to calculate ^{18}O EIEs as the product of reduced partition function ratios (ZPE × EXC × MMI) corresponding to zero-point

energy (ZPE), vibrational excitation energy (EXC) and the mass and moments of inertia (MMI). Calculations of ^{18}O KIEs are generally less accurate due to the uncertainty of intermediate and TS structures. In Eq 2, the $^{18}K^{TS}$ is formulated analogously to the ^{18}O EIE, except it contains a vibrational product (VP) with one less ratio of frequencies than the MMI. The $^{18}\nu_{RC}$ reflects the ratio of imaginary modes that define the TS along the reaction coordinate. When ^{18}O can adopt multiple positions in the precursor or TS, the KIEs are Boltzmann-weighted.[4] Such corrections are typically very small and within the experimental error limits.

I. Mechanistic Implications:

The competitive ^{18}O KIEs are derived from multiple independent measurements at variable catalyst turnover numbers (TONs), from one to ten or greater. This is a major difference from the ^{18}O-isotope labeling experiments that are constrained to probe a single stoichiometric reaction because of H_2O exchange.[21a,22a,23c] The isotope fractionation measurements actually require rapid H_2O exchange via the ruthenium(II) or ruthenium(III) dioxygen states during catalytic turnover. That the competitive ^{18}O KIEs are independent of CAN concentration and TON strongly indicates water oxidation by a single mechanism. This has been a major concern for catalysis by the classic **Ru$_2^{BD}$**, where studies have suggested at least one other reaction pathway in competition with **WA**.[22] Mechanisms of catalysis initiated by **Ru**, **Ru$_2^{BD}$** and **Ru$_2^{Hbpp}$** have been intensively studied,[21-23] and were selected for the present investigations on this basis. Rate-limiting **WA** has been proposed for **Ru**-initiated catalysis (Scheme 3).[12,42] The predominance of a similar **WA** mechanism assisted by two explicit water molecules has been proposed for **Ru$_2$BD** (Scheme 4).[43] In contrast, **Ru$_2^{Hbpp}$** has been proposed to react by an **OC** mechanism, via the IV,IV oxidation state.[23] Reactions via the IV,IV and IV,V oxidation states are considered below (Scheme 5).

Scheme 3. Minimal mechanism of **WA** during **Ru**-initiated water oxidation.

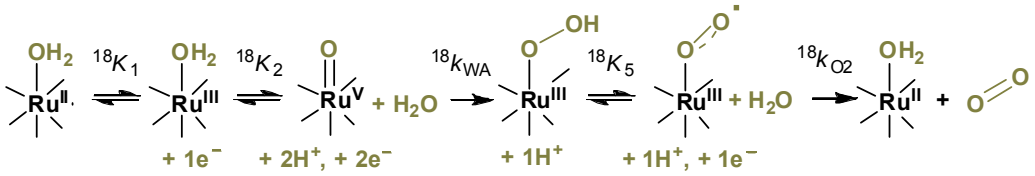

Scheme 4. Minimal mechanism for **WA** during **Ru$_2^{BD}$**-initiated water oxidation. Di-ruthenium (II, IV) formed upon O_2 loss may precede regeneration of the more stable (III,III) oxidation state.

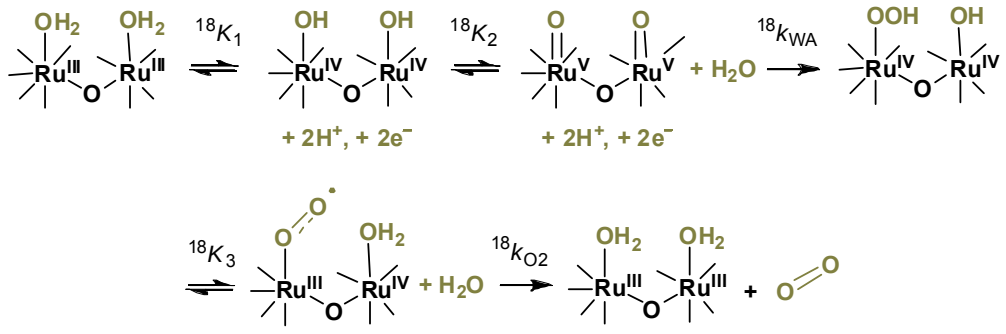

Scheme 5. Minimal mechanism of **OC** during $\mathbf{Ru_2}^{\mathbf{Hbpp}}$-initiated water oxidation via intermediates in IV,IV (a) or IV,V (b) oxidation states.

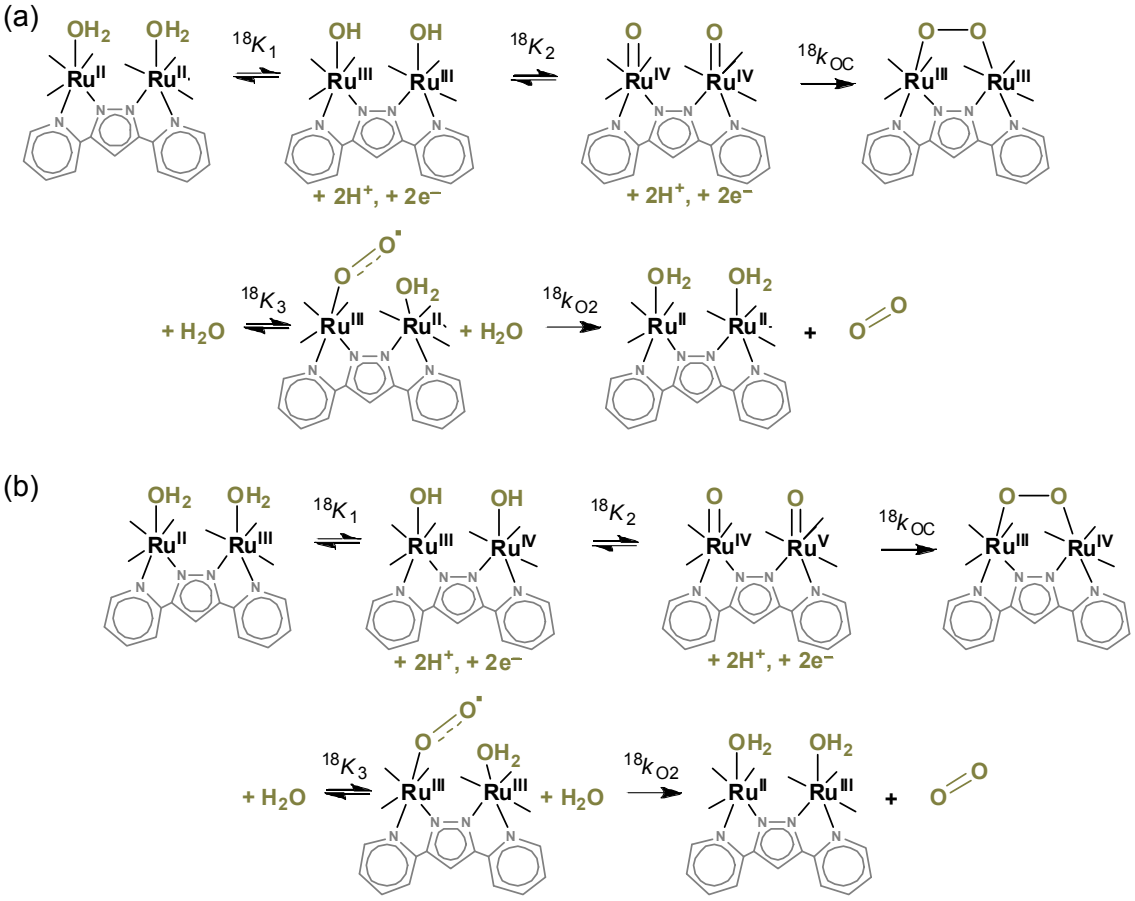

J. Transition States for O-O Bond Formation:

A summary of numerous DFT calculations is provided below with the results found to agree with experimental data highlighted. As noted in the preceding discussions,[4,12b] spin-state and solvation have little to no effect on the ^{18}O KIEs. Therefore, results are described only for the lowest spin states in the gas phase.

Three **WA** TSs with distinct hydrogen-bonding patterns (involving four or five explicit H_2O molecules) were identified for catalysis initiated by **Ru** (Figure 8). At the M06-L level of theory, **WA**[4a] has the most advanced or product-like TS. The Ru−O bond lengthens from 1.688 Å in the ruthenyl precursor to 1.875Å in **WA**[4a] versus 1.747 Å in **WA**[4b] and 1.743 Å in **WA**[5] while the O−O bond distance is 1.590 Å in **WA**[4a] versus 1.962 Å in **WA**[4b] and 1.974 Å in **WA**[5]. The calculated free energy barriers, $\Delta G^{\ddagger}$(O−O), fall within a narrow range of 19 to 23 kcal mol^{-1},

close to the experimental estimate of 18.9 kcal mol^{-1}. Despite the larger $\Delta G^{\ddagger}$(O−O), the experimental ^{18}O KIE = 1.0306 ± 0.0004 is best modeled by **WA^{4a}** with calculated isotope effects of 1.0240 (*m*PW) and 1.0303 (M06-L) in the gas phase. Re-optimization in an aqueous continuum had no significant effect on the ^{18}O KIEs. Considering the nature of spin and solvent corrections, the ^{18}O KIE is expected to be calculated to a higher level of accuracy than the $\Delta G^{\ddagger}$(O−O). This is consistent with the observation that the barrier associated with **WA^{4a}** is higher than the alternative TS configurations.

Figure 8. Precursor and transition states for catalytic water oxidation initiated by **Ru** at the M06-L level of theory. Calculated ^{18}O KIEs are provided (*m*PW / M06-L) along with the imaginary frequency of the light isotopologue.

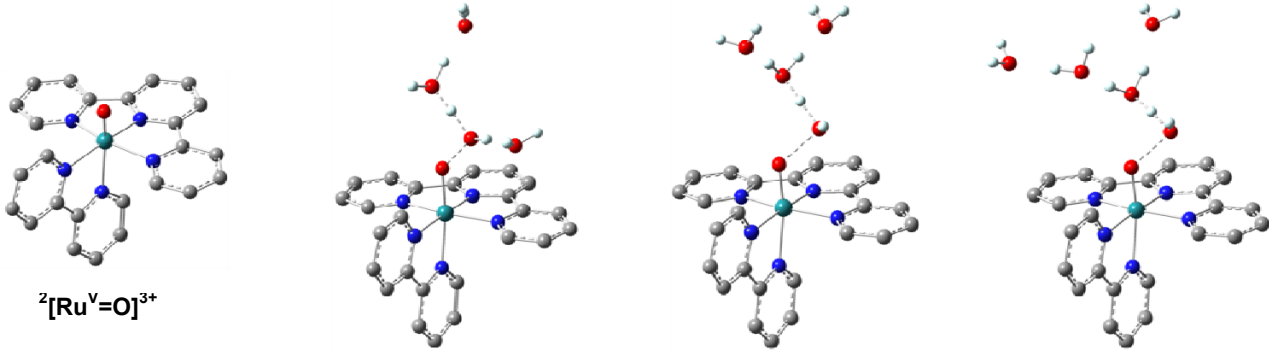

^{2}[Ru^{V}=O]$^{3+}$ WA^{4a}(411.62i cm^{-1}) WA^{4b} (307.93i cm^{-1}) WA^{5} (327.33i cm^{-1})

1.0240 / 1.0303 — / 1.0158 1.0106 / 1.0113

The blue dimer,[44] **Ru$_2^{BD}$**, is converted into di-ruthenyl intermediates in the (IV, V) and (V, V) oxidation states during catalysis.[45,46] DFT calculations were undertaken for reactions of (V,V) intermediate in the unrestricted singlet state assuming strong anti-ferromagnetic coupling. In contrast to results of isotope labeling studies,[22] a single type of mechanism is indicated by the ^{18}O KIE = 1.0169 ± 0.0003 under catalytic conditions. Two distinct water attack TSs, **WA^{1}** and **WA^{2}**, featuring one or two explicit H_2O molecules, were identified and compared to a new TS identified for **OC** at the M06-L level of theory (Figure 9). The same **OC** transition state could not be identified with the *m*PW functional, however, raising questions concerning this saddle-point structure and its $\Delta G^{\ddagger}$(O−O).

The most product-like TS, exhibiting the best agreement with the experimental ^{18}O KIE, is associated with **WA^{2}**. Calculations in the unrestricted singlet and triplet states gave indistinguishable results. In the former, the precursor is a staggered conformer with a Ru−O bond length of 1.723 Å and O−O distance of 5.112 Å. In the TS, the Ru−OO bond length is expanded to 1.931 Å, which is significantly larger than the Ru−OH bond length of 1.770 Å, while the O−O bond length is contracted to 1.569Å. Similar behavior is observed for the eclipsed conformer in the triplet state where the initial Ru−O bond lengths are 1.764 Å and 1.697 Å and

the O−O distance is 2.827 Å. In the TS, the Ru−OO bond length is 1.935 Å, the Ru−OH bond length is 1.770 Å and O−O bond length is 1.560 Å.

The $\Delta G^{\ddagger}$(O−O) for the favored TS **^{1}WA^{2}** (≅ 36.5 kcal mol^{-1}) is more than two times greater than the experimentally determined barrier, yet as mentioned above this energy is unreliable due to the inadequate nature of spin and solvation corrections. The energy barrier is larger than that calculated for **^{1}OC** (≅ 27.3 kcal mol^{-1}), however, the latter is suspect because it could not be identified with the *m*PW functional. The $\Delta G^{\ddagger}$(O−O) for **^{1}WA^{1}** (≅ 46.8 kcal mol^{-1}) is significantly disfavored, consistent with independent computational results.[43] Despite the overestimated TS energies, the results of *m*PW and M06-L calculations for **^{1}WA^{2}** give an average ^{18}O KIE of 1.0161, in good agreement with the measured ^{18}O KIE.

Figure 9. Precursor and transition states for catalytic water oxidation initiated by **Ru$_2^{BD}$** at the M06-L level of theory. Calculated ^{18}O KIEs are provided (*m*PW / M06-L) along with the imaginary frequency of the light isotopologue.

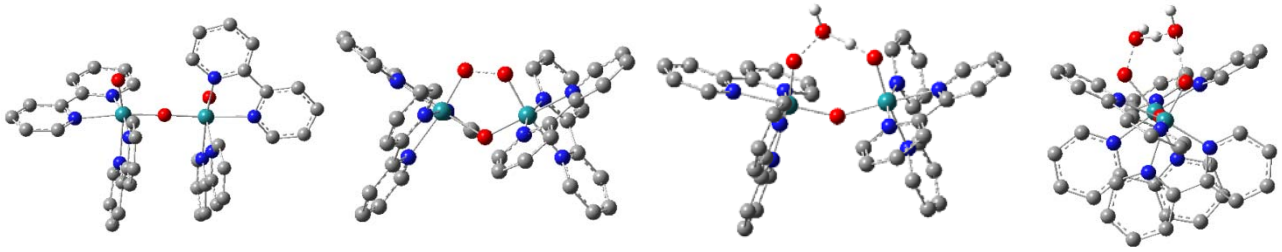

^{1}Ru$_2^{BD}$ (V,V)	**^{1}OC (345.78i cm^{-1})**	**^{1}WA^{1} (958.40i cm^{-1})**	**^{1}WA^{2} (571.79i cm^{-1})**
	— /1.0393	1.0012/ 1.0071	1.0151 / 1.0172

Catalysis initiated by the geometrically constrained di-ruthenium (II, II) complex, **Ru$_2^{Hbpp}$**, is considered to proceed via two different oxidized precursors, despite the observation that the ^{18}O KIE = 1.0347 ± 0.0004 is the same when analyzed for a single turnover up to 40 TONs. The O−O bond forming reactions of di-ruthenyl intermediates via the (IV, IV) and (IV, V) oxidation states are modeled in Figure 9. TSs for **OC**, **WA^{1}** and **WA^{2}** were compared with no significant deviations in the ^{18}O KIEs indicated for the low-spin and high-spin states.

As in the calculations described above, the most advanced TSs exhibit ^{18}O KIEs that show the best agreement with experimental values. Consistent with the absence of solvent deuterium isotope effects, these TSs correspond to **OC**. Reaction of the (IV, IV) intermediate in the unrestricted singlet state (**^{1}OC**) involves elongation of the Ru−O bond from 1.757 Å to 1.840 Å and an O−O bond contraction to 1.715 Å. Similar behavior characterizes reaction of the (IV, V) intermediate via the low-spin doublet state (**^{2}OC**) where the precursor Ru−O bonds elongate from 1.724 Å and 1.767 Å to 1.808 Å, while the O−O bond contracts to 1.691 Å.

For reactions of **Ru$_2^{Hbpp}$**, TSs assigned to **OC** are substantially lower in energy than the **WA^{1}** and **WA^{2}** alternatives. The $\Delta G^{\ddagger}$(O−O) for **^{1}OC** and **^{2}OC** are both ~14 kcal mol^{-1} and somewhat lower than the experimentally determined barrier. The **^{1}WA^{1}** and **^{1}WA^{2}** TSs attained from the di-

ruthenium (IV, IV) bis-oxo intermediate are 30-40 kcal mol^{-1} higher in energy than **^{1}OC** and exhibit ^{18}O KIEs too small to be reconciled with experiment. **^{2}WA^{1}** and **^{2}WA^{2}** TSs calculated from the di-ruthenium (IV, V) bis-oxo intermediate are 13-14 kcal mol^{-1} higher in energy than **^{2}OC** and the ^{18}O KIEs are smaller than those observed. Assuming a reaction via **^{1}OC** or **^{2}OC**, the ^{18}O KIE should lie between the limits of 1.031 predicted *m*PW by and 1.045 predicted by M06-L, just as observed experimentally. If the ^{18}O KIEs for **Ru$_2^{Hbpp}$** were significantly smaller than the values calculated for O−O formation, O_2 release could reflect a small fraction of the turnover-limiting step due to a contribution from an inverse ^{18}O KIEs approaching unity.[29c]

Figure 10. Precursor and transition states for catalytic water oxidation initiated by **Ru$_2^{Hbpp}$** at the M06-L level of theory. Calculated ^{18}O KIEs are provided (*m*PW / M06-L) along with the imaginary frequency of the light isotopologue.

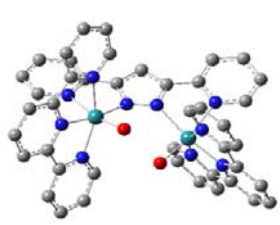

^{1}Ru$_2^{Hbpp}$ (IV,IV)

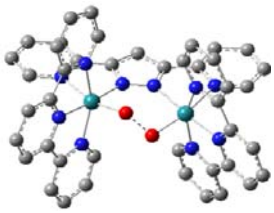

^{1}OC (IV,IV)
(396.84i cm^{-1})

1.0311 / 1.0447

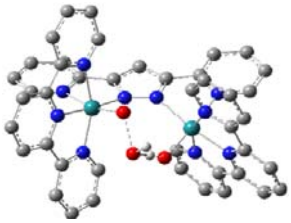

^{1}WA^{1} (IV,IV)
(1436.74i cm^{-1})

0.9995 / 0.9987

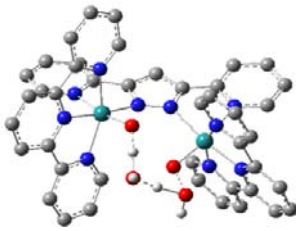

^{1}WA^{2} (IV,IV)
(1412.47i cm^{-1})

1.0020 / 1.0046

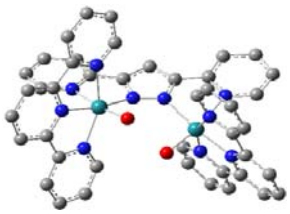

^{2}Ru$_2^{Hbpp}$ (IV,V)

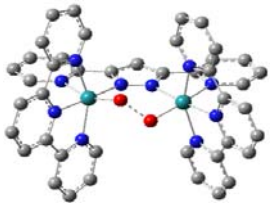

^{2}OC (IV,V)
(337.18i cm^{-1})

— / 1.0445

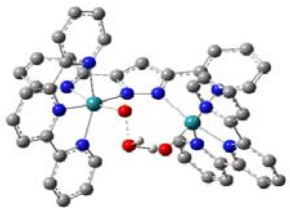

^{2}WA^{1} (IV,V)
(228.49i cm^{-1})

1.0235 / 1.0344

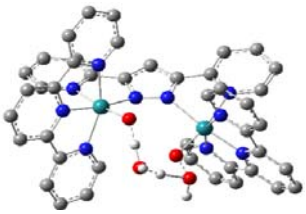

^{2}WA^{2} (IV,V)
(437.40i cm^{-1})

1.0241 / 1.0234

Conclusions:

Studies of stoichiometric and catalytic water oxidation by iron and ruthenium oxo complexes have demonstrated that competitive oxygen-18 isotope fractionation affords ^{18}O KIEs that serve as probes of O−O bond formation mechanisms. Experimental results for monomeric and dimeric complexes are reproduced using disparate levels of DFT to provide optimized structures, together with the mass-dependent normal and imaginary vibrational modes. Vibrational

frequencies of precursor and transition states used in the ^{18}O KIE calculations predict large normal effects (ca. 1.030-1.045) for oxo-coupling and smaller effects (ca. 1.000-1.030) for water attack mechanisms**.** Thus, the ^{18}O KIEs provide compelling evidence that O−O bond forming steps limit the turnover rate constants of water oxidation catalysis.

IV. Proposed Project Objectives:

Findings in photosynthesis research have shaped our understanding of how transition metal oxo species act as "artificial" photosynthetic catalysts capable of water oxidation. Following from the previous project period, we plan to continue to investigate the connection between biological and synthetic inorganic catalysts, while establishing new ways of probing mechanisms using ^{18}O KIEs. Future investigations will address the physical origins of ^{18}O KIEs at a greater level of detail on a wider range of photo-catalytic and electro-catalytic systems.

Objective 1. Driving-Force Dependence of Kinetics and ^{18}O KIEs.

Background:

Systematic studies of kinetics and ^{18}O KIEs at variable electrochemical driving-force are proposed to provide insight as to the origin of the intrinsic barrier or over-potential for water oxidation, so that catalysts that exhibit lower activation energies can be designed. Terms such as reorganization energy (λ) defined in Electron Transfer Theory will be used to characterize contributions to the intrinsic barrier. In the intersecting parabola diagram shown to the left, the electronic transition energy (E_{op}) is equated to the sum of the $\Delta G°$ and λ. The intersection of the two harmonic wells defines the free energy barrier, $\Delta G^{‡} = \lambda/4(1+ \Delta G°/\lambda)^2$. The λ term contains outer-sphere (solvent) and inner-sphere (bonding) contributions. The latter can be calculated using DFT to determine the energy associated with change in bond distances and force constants. Minimization of these changes could enhance rates of O−O bond formation during catalysis.

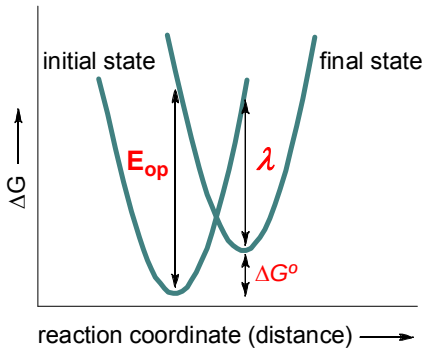

Proposed Studies:

The ruthenium complexes[21-23] examined during the previous project period are amenable to studying kinetics and ^{18}O KIEs under electro-catalytic conditions as are the iridium, iron and manganese complexes described below. Our recent preparation of an aqueous-soluble organometallic iridium complex, related to known pre-catalytic species,[47,48] will be the subject of initial investigations of how thermodynamics affects rates and ^{18}O KIEs associated with catalytic water oxidation. Studies at variable pH will also be undertaken to probe how kinetics and mechanisms of O−O bond formation may change. The results will provide insights as to the origin of intrinsic barriers for specific mechanisms.

The complex $[Cp^*Ir(bpy)(H_2O)](ClO_4)_2$, where Cp* = 1,2,3,4,5 permethylcyclopentadienyl, referred to throughout as **Ir-Aq**, has been crystallized from methanol and water at ambient

temperature (Figure 11). **Ir-Aq** is ca. 100-times more soluble than related organometallic iridium complexes with phenyl pyridine (ppy) in place of the bpy ligand and chloride in place of H_2O. ^1H NMR analysis at millimolar **Ir-Aq**, in the presence of 5 to 25 equivalents of CAN, reveals that ca. 20% of the starting material undergoes Cp* oxidation and 50% is converted to paramagnetic species on the timescale of several minutes. Thus, **Ir-Aq** decomposition has no bearing on the ^{18}O KIE and steady-state kinetic experiments described below and in a recent manuscript.[49]

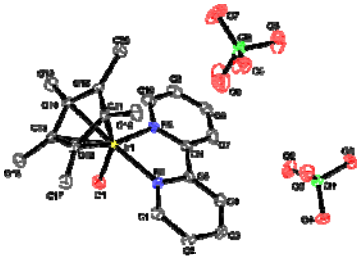

Figure 11: ORTEP of $[Cp^*Ir(bpy)(H_2O)](ClO_4)_2$, where Cp* = permethcyclopentadienyl, is drawn with 50% ellipsoid probability and hydrogen atoms omitted. The following bond lengths are in Å: Ir1-N2 2.081(2), Ir1-N1 2.107(2), Ir1-O1 2.152(2). Selected bond angles are given in (°): N2-Ir1-N1 76.92(9), N1-Ir1-O1 84.61(9), N2-Ir1-O1 84.18(9).

Dynamic light scattering measurements have also been performed as control experiments, under the conditions used to probe rate constants and ^{18}O KIEs, and no evidence obtained for nanoparticulate formation. Increasing the **Ir-Aq** concentration by a factor of 10^3 (to the millimolar range) does result in nanoparticle formation, however, over hundreds of seconds. The conclusion that nanoparticles do not influence the steady-state kinetic parameters and ^{18}O KIEs is reinforced by electronic absorption measurements that reveal formation of a tight isosbestic point near 345 nm concomitant with a slight increase in optical density at 585 nm.

Kinetics and ^{18}O KIEs on CAN-dependent water oxidation catalysis have been determined for **Ir-Aq** and compared to Cp*Ir(ppy)(Cl) and $[Cp^*Ir(Cl)(\mu\text{-}Cl)]_2$, which undergo chloride displacement by water. All complexes exhibit k_{cat} values between 0.1 and 0.2 s^{-1} in 0.1 M $HClO_4$ with CAN as the oxidant.[49] Furthermore, ^{18}O KIEs are invariant to CAN concentration and TON strongly suggesting that the catalytic species is unperturbed by side-reactions that could occur with aggregates of Ce^{IV} species (cf. the studies of **Ru** catalysis in the previous results section).

The data shown in Figure 12 indicate that **Ir-Aq** reacts with a solvent deuterium kinetic isotope effect on k_{cat} = 1.85 ± 0.08 (as well as k_{cat}/K_{CAN}) and an ^{18}O KIE = 1.0231 ± 0.0019 in 0.1M $HClO_4$ at pH 1.0. The size of the solvent deuterium KIEs and ^{18}O KIE suggest that **Ir-Aq** reacts by rate-limiting O−O bond formation via a **WA** transition state. As in the experiments with **Ru** and $\mathbf{Ru_2^{BD}}$ described above, a diminution of the ^{18}O KIE to 1.0141 ± 0.0010 is observed when **Ir-Aq** is reacted with photo-generated $[Ru(bpy)_3]^{3+}$ in 0.05M KP_i at pH 7.2 indicating a change in the transition state and/or the rate-determining step.

Figure 12. (a) Steady state kinetics in H_2O (circles) and D_2O (squares) and (b) ^{18}O KIEs at pH 1 with variable concentrations of CAN (circles) and $[Ru^{III}(bpy)_3]^{3+}$ at pH 7.2 (squares).

(a)

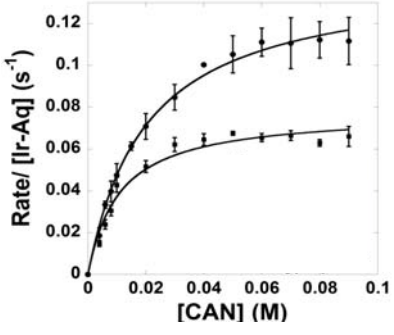

(b)

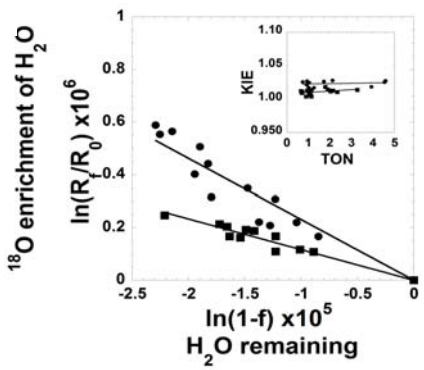

Computational studies are underway to model the ^{18}O KIEs exhibited by **Ir-Aq** at low pH in relation to the $[Cp^*Ir(Cl)(\mu\text{-}Cl)]_2$ and $Cp^*Ir(ppy)(Cl)$ pre-catalysts. Significantly smaller ^{18}O KIEs of 1.0120 ± 0.0008 and 1.0137 ± 0.0008 were determined for the respective complexes from the data shown in Figure 13. Catalysis initiated by $Cp^*Ir(ppy)(Cl)$ is also characterized by a solvent deuterium isotope effects of 1.8 ± 0.1 on k_{cat} (and k_{cat}/K_{CAN}), indicating a rate-limiting step similar to that observed for **Ir-Aq**. A difference in reaction driving-force is a potential explanation for the variation in observed ^{18}O KIEs. This hypothesis will be tested as described below.

Figure 13. Isotope fractionation data for $[Cp^*Ir(Cl)(\mu\text{-}Cl)]_2$ (squares) and $Cp^*Ir(ppy)(Cl)$ (circles) at variable CAN concentration and pH 1.0. Kinetic data are also shown for the latter.

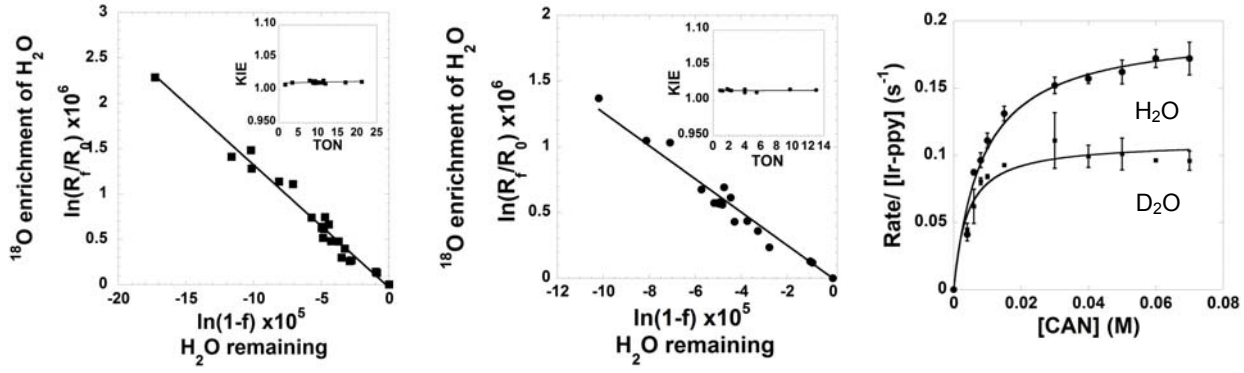

^{18}O KIEs will be determined for **Ir-Aq** at variable $\Delta G°$ by controlled potential electrolysis, initially at pH 1, for comparison to oxidations by CAN. A gas-tight electrochemical cell[50] will serve as the reaction chamber interfaced with the apparatus in Figure 1. This modification will facilitate the determination of ^{18}O KIEs from the O_2 produced upon bulk electrolysis.[51] Electrocatalysis of water oxidation by **Ir-Aq** will also be examined using cyclic voltammetry at varying pH, which should also affect the $\Delta G°$ of reaction. Changing the pH could also affect the identities of catalytic intermediates, which will be tested using various spectroscopic techniques on relevant timescales. **Ir-Aq** is likely to exhibit well-defined electrocatalytic behavior in view of results obtained with related Cp^*Ir^{III} pre-catalysts that homogenously produce O_2.[52,53,54] The driving-force dependence of k_{cat} (or $\Delta G^{‡}$) and the ^{18}O KIE will be thus be determined. Further analysis using DFT will reproduce the experimental parameters and determine the λ, directly related to the intrinsic barrier for specific mechanisms of O−O bond formation.

Computational modeling of reactive species and transition states during catalysis by **Ir-Aq** will be performed in collaboration with Prof. Rajeev Prabhakar (University of Miami). Due to the time-intensive nature of the calculations, a subcontract for three months of Prof. Prabhakar's salary is requested. Prabhakar excels in constructing models that can explain the influence of hydrogen bonding in redox reactions.[14] Initially, DFT studies will focus on the proposed rate-

limiting **WA** step in **Ir-Aq** catalysis. The TS will be modeled considering the influence of explicit water molecules as well as nitrate and phosphate ions present in reactions at pH 1.0 and 7.2. ^{18}O KIEs on H_2O coordination[26] to Ir and IrO_2 species, oxidation by electron transfer or proton-coupled electron transfer[14,27,28] and O_2 release[29] steps will also be evaluated for comparison. Modeling the variation in ^{18}O KIEs with $\Delta G°$ determined electrochemically will address the origin of the intrinsic barrier ($\lambda/4$), defined according to Electron Transfer Theory.

Objective 2. Probing Catalytic Intermediates Capable of Reversible O−O Bond Formation.

Background:

The thermodynamics associated with the O−O bond formation step in water oxidation has been difficult to address. In some computational studies, O−O bond formation is the highest energy transition state along the reaction coordinate, whereas in others, it is of lower energy than the reactant(s). In the latter case, a kinetically reversible process would give intermediates that are expected to exhibit small and possibly inverse ^{18}O KIEs.[10] The experiments proposed below will illuminate the factors that allow reversible O−O bond making and breaking via a transition metal hydroperoxo intermediate. On this note, we have previously discovered such behavior in an enzymatic transformation.[6] In horseradish peroxidase, an iron(III) hydroperoxo intermediate is formed prior to proton-induced O−O heterolysis, which reversibly forms an iron(IV) porphyrin π-cation radical and H_2O (Figure 14). Experimentally the evidence for reversible bond-breaking comes from the scrambling of ^{18}O-labeled water into the unreacted H_2O_2. This result is consistent with DFT calculations, suggesting that $\Delta G°$ close to 0 kcal mol^{-1}.[6]

Figure 14: Isotope fractionation results for horseradish peroxidase catalyzed H_2O_2 reduction at natural abundance (a) and in 1.2% ^{18}O-enriched water (b). The DFT calculated energies for the O−O heterolysis and the ^{18}O KIE = 1.0127 ± 0.0008 are in kcal mol^{-1}.

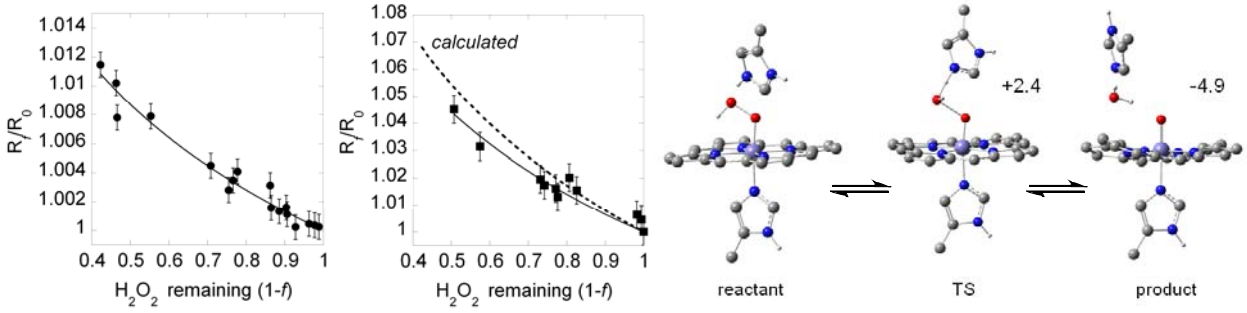

Proposed Studies:

Geometrically constrained complexes that cannot undergo oxo-coupling are proposed to undergo O−O bond formation by water attack mechanisms.[55] We will examine whether these reactions proceed via transition metal hydroperoxo intermediates. Such a result was predicted for $[Mn^{III,IV}(\mu\text{-}O)(tpy)(OH_2)]_2(NO_3)_3$, the original synthetic model for OEC catalysis.[56]

Preliminary results suggest that $[Mn^{III,IV}(\mu\text{-}O)(tpy)(OH_2)]_2^{3+}$ undergoes oxidation by CAN to form a di-manganyl (IV,V) intermediate followed by **WA**, as depicted in the first step of Figure

15. Analysis of the O_2 produced indicates an ^{18}O KIE = 1.0073 ± 0.0022, which is consistent with computed ^{18}O KIEs for **WA** and inconsistent with the larger ^{18}O KIEs expected for **OC**.[4,12b] Although further experiments are needed to evaluate the mechanistic origin of the ^{18}O KIE on $[Mn(\mu\text{-}O)(tpy)(OH_2)]_2^{3+}$ mediated water oxidation by CAN, it is worth noting that a **WA** transition state calculated by Siegbahn et al.[57] predicts an ^{18}O KIE = 1.022. This value was obtained by re-optimizing the B3LYP-derived transition state using the calibrated *m*PW protocol to determine the normal and imaginary vibrations. Thus, new DFT calculations will be undertaken to model the experimental result, which may reflect a reversible O−O bond formation followed by an irreversible Mn−OOH oxidation or O_2 release step.

We have found that $[Mn^{III,IV}(\mu\text{-}O)(tpy)(OH_2)]_2(NO_3)_3$ rapidly oxidizes H_2O_2 to form stoichiometric O_2, while presumably undergoing reduction to a di-manganese (II,III) species. An ^{18}O KIE = 1.0107 ± 0.0017 was determined on this reaction. Incidentally, the transition state for O−O bond breaking within the Mn−OOH intermediate is related to O−O bond formation by the principle of microscopic reversibility. Thus, the transition state for may be the same as that for the water oxidation reaction described above, *i.e.*, a step after **WA** upon a di-mangangyl (IV,V) intermediate. Experiments will test the reversibility of O−O bond-breaking within the proposed Mn−OOH intermediate shown in Figure 15, by generating this species from $[Mn^{III,IV}(\mu\text{-}O)(tpy)(OH_2)]_2(NO_3)_3$ and H_2O_2 in the presence of natural abundance and ^{18}O-enriched water. Scrambling of ^{18}O into the Mn−OOH unit will be probed by IRMS analysis of $^{18}O/^{16}O$ in the unreacted H_2O_2 or O_2 formed, as described above.[6]

Figure 15. Reactions of $[Mn(\mu\text{-}O)(tpy)(OH_2)]_2^{3+}$ that form O_2 via a hydroperoxo intermediate.

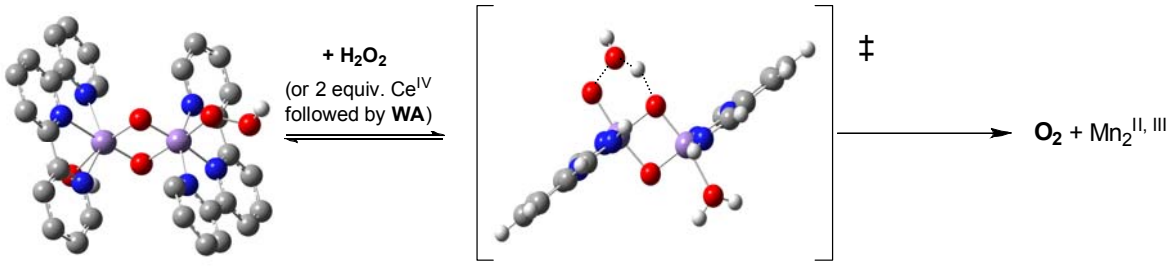

To investigate the reversibility of O−O bond formation in systems with low intrinsic barriers to **WA**, we will analyze monomeric iron complexes that contain unoccupied cis-coordination sites.[58] Experiments are proposed with iron(II) TMPA and TEPA complexes with triflate or perchlorate counterions, where TMPA = tris(2-pyridylmethyl)amine) and TEPA = tris(2-pyridylethyl)amine. These complexes can be generated in oxidation states between II and IV,[59] allowing ^{18}O KIEs on stoichiometric and catalytic reactions to be examined and evidence obtained for a common rate-limiting step. Given the $\Delta E°$ = 1.0 V difference in redox potentials of copper(II) TMPA and TEPA complexes,[60] changing the ligand could result in a crossover from reversible to irreversible mechanism of **WA** upon a transient iron oxo species.

$[Fe^{II}(TMPA)]^{2+}$ has been reported to mediate water oxidation by $NaIO_4$ near neutral pH.[58] We have found that this complex also initiates water oxidation in the presence of excess CAN at

pH 1 and 22 °C. Normal saturation kinetic behavior is observed upon increasing the CAN concentration in Figure 16, where k_{cat} is characterized by a solvent deuterium kinetic isotope effect of 1.8 ± 0.2. Under the analogous conditions an ^{18}O KIE = 1.0251 ± 0.0017 was determined consistent with a **WA** mechanism, as proposed for related Fe^{IV} complexes.[61]

Figure 16. (a) The initiator of water oxidation catalysis shown with the accompanying steady-state kinetics in H_2O (circles) and D_2O (squares) (b) and isotope fractionation (c).

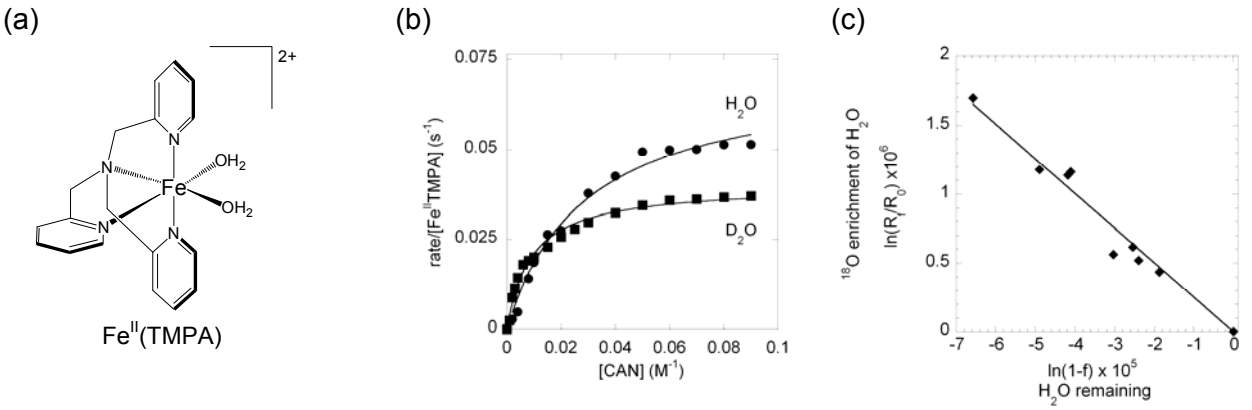

As outlined above for the di-manganese complex,[56] attempts will be made with the iron(II) and iron(III) complexes of TMPA and TEPA to determine ^{18}O KIEs on H_2O_2 oxidation to O_2 in natural abundance and ^{18}O-enriched water. These experiments will illuminate the reversibility of O−O bond-formation within potential (hydro)peroxide intermediates in water oxidation catalysis. It would be surprising if scrambling was observed, however, in light of the size of the solvent deuterium isotope effect and ^{18}O KIE determined at pH 1, which implicate irreversible **WA**. These studies will be undertaken in concert with DFT modeling efforts to determine the origin of the ^{18}O KIE due to O−O bond formation within monomeric iron complexes. Large ^{18}O KIEs predicted for the analogous reaction in computational studies of ferrate[4] suggest that O−O bond formation via a putative $[Fe^{IV}=O(OH_2)(TMPA)]^{2+}$ intermediate may be only partially rate-limiting.

Objective 3. Characterization of Photocatalysis by Insoluble Transition Metal Oxides.

Background:

Photo-electrochemical cells are capable of generating current and/or hydrogen from visible light. Transition metal oxide semiconductors are routinely used in the fabrication of such photo-electrodes and solar cells. Currently photo-electro-catalytic cells have surpassed the 10% quantum efficiency cutoff needed to be economically viable, yet problems remain due to corrosion by the aqueous surroundings. A new specification referred to as “service life” has been adopted, meaning that the catalyst should retain activity for >10,000 hours.[62]

The present objective is intended to build greater knowledge of how ^{18}O KIEs may be used to probe transition metal oxide reactivity in complex environments. This aim coincides with the need to understand mechanistic underpinnings of water oxidation at photo-activated metal oxide

surfaces, to improve existing technologies as well as to develop new ones. A primary focus will be upon tungsten trioxide, which is one of the most thoroughly studied solid-state photocatalysts for water oxidation to date.[7,63,64]

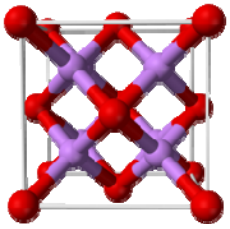

Tungsten trioxide (WO_3) is an n-type semiconductor with band gap of ca. 2.7 eV.[63] It has been characterized in various crystalline and amorphous states.[7] Catalytic water oxidation by orthorhombic WO_3 (shown to the left) exhibits a reasonable quantum efficiency and robustness, producing O_2 upon irradiation over the course of several hours. Thus, its mechanism of action is critical to the design of industrial catalysts that can use visible light for the production of electricity or hydrogen.

Proposed Studies:

Orthorhombic crystals will be prepared and characterized,[64] by XRD, SEM and TEM (all available through facilities at Johns Hopkins). Further tests of structural changes within the WO_3 will be conducted upon increasing reaction timescales and catalyst turnover numbers. We have already confirmed that ^{18}O KIEs can be determined on aqueous dispersions of WO_3 of known morphology and size solutions containing silver(I) or iron(III) salts act as electron acceptors. Photocatalytic O_2 production has been detected over the course of hours when irradiated between 350 nm and 450 nm using a 1000W Hg/Xe lamp equipped with a dichroic mirror. Yields of O_2 depend on the amount of WO_3 and the concentration of electron acceptor. Minimal background production of O_2 occurs in the absence WO_3 when solutions of the electron acceptors are photolyzed under the conditions described. Collection of O_2 has been accomplished using the apparatus in Figure 1, where the photocatalysis takes place in the bubbler compartment under reduced pressure and He flow. This experimental setup allows O_2 to be collected, pressures analyzed and samples prepared for IRMS, as outlined above. Steady-state kinetic measurements of solvent deuterium isotope effects will be undertaken to complement the analysis of ^{18}O KIEs and allow evaluation of the rate-limiting step occurring on the WO_3 surface via the proposed minimal mechanism:

$$2\ W{=}O^* + H_2O \rightarrow WOOH + WOH$$

$$WOOH + WOH \rightarrow WOO + WOH_2$$

$$WOO + H_2O \rightarrow WOH_2 + O_2$$

Based on the conduction band energy of WO_3, water association should result in initial oxidation by proton-coupled electron transfer or hydrogen atom transfer to surface W=O sites. These reactions are thermodynamically downhill and, therefore, unlikely to be rate-limiting. Subsequent O–O coupling is proposed to involve hydroxyl/hydroxide attack upon a tungsten oxo species, concomitant with hydrogen atom/proton transfer to an adjacent site. This hydroperoxide intermediate could spontaneously transfer hydrogen to an adjacent surface site. The displacement of O_2 by H_2O may occur in the rate-limiting step. As described above, experimental results will be compared to DFT calculations used to model relevant mechanisms.

Concluding Comments:

We have obtained a number of experimental results that support the utility of ^{18}O KIEs as mechanistic probes of O−O bond forming steps during catalytic and stoichiometric water oxidation reactions. In tandem, we have shown how DFT-modeling of transition states can be used to predict measured ^{18}O KIEs, thus illuminating mechanisms of O−O bond formation. We plan to continue to drive this effort forward by examining a variety of new systems for which preliminary data have been obtained. The proposed project period will extend studies to electro-catalytic reactions. These experiments will provide knowledge of intrinsic reaction barriers needed to improve catalytic performance. Oxygen isotope fractionation will also be applied to examine thermodynamics of O−O bond forming reactions where DFT methods fail to predict energy barriers. Finally, experiments on an established solid-state photo-catalyst are planned to obtain mechanistic insights into reactions on metal oxide surfaces.

Appendix 1: Biosketch

Justine P. Roth Ph.D.

Associate Professor of Chemistry
Johns Hopkins University, 3400 N. Charles Street, Baltimore, MD 21218
Phone: (410) 516-7835, Fax: (410) 516-8420, E-mail: jproth@jhu.edu
www.jhu.edu/~chem/roth/index.html

I. Education and Training:

2000-2003	NIH Postdoctoral Fellow, University of California, Berkeley
1995-2000	Ph. D. Chemistry, University of Washington, Seattle
1990-1994	B.S. Chemistry, University of Florida, Gainesville

II. Research and Professional Experience:

2009-present	Tenured Associate Professor of Chemistry, JHU
2007-present	Program for Molecular Biophysics (PMB-JHU)
2005-present	Chemistry-Biology Interface Program (CBI-JHU)
2003-2009	Assistant Professor of Chemistry, JHU

III. Honors and Awards:

2009-2011	Dreyfus Environmental Chemistry Award
2008	Camille Dreyfus Teacher Scholar Award
2007	Alfred P. Sloan Research Fellowship Award
2006	Research Corporation Cottrell Scholar Award
2006	Paul D. Saltman Award Lecture, *Metals in Biology* GRC
2005	NSF CAREER Award
2004	ACS PROGRESS/Dreyfus Foundation Lectureship
2004	Synlett and Synthesis New Faculty Journal Award
2000-2003	National Institutes of Health Postdoctoral Fellowship

IV. Synergistic Activities:

2011-present	*Accounts of Chemical Research* Ed. Advisory Board
2011	NSF Chemistry of Life Processes Panel
2010-2011	Department of Energy (DOE) Early Career Panel
2010	R32 NIH Postdoctoral Fellowship Panel
2008-2010	NSF CAREER Award Panel in the MPS Directorate
2013	NSF CAREER Award Panel in the MCB Directorate

V. Publications (*indicates DOE support):

(0*) "Oxygen-18 Kinetic Isotope Effects on Water Oxidation by Monomeric and Dimeric Ruthenium Catalysts." Angeles-Boza, A. M. Ertem, M. Z.; Sarma, R. Ibañez, C. H.; Maji, S.; Llobet, A.; Cramer, C. J. Roth, J. P. *Chem. Sci.* **2013** submitted.

(1*) "Experimental and Computational Evidence of Metal-O_2 Activation and Rate-Limiting Proton-Coupled Electron Transfer in a Copper Amine Oxidase." Liu, Y.; Mukherjee, A.; Nahumi, N.; Ozbil, M.; Brown, D.; Angeles-Boza, A. M.; Dooley, D. M.; Prabhakar, R.; Roth, J. P. *J. Phys. Chem. B* **2013**, *117*, 218-229 DOI: 10.1021/jp312148

(2*) "Studies of the Di-iron(VI) Intermediate in Ferrate-Dependent Oxygen Evolution from Water." Sarma, R.; Angeles-Boza, A. M.; Brinkley, D. W.; Roth, J. P. *J. Am. Chem. Soc.* **2012**, *134*, 15371-15386.

(3*) "Oxygen Kinetic Isotope Effects upon Catalytic Water Oxidation by a Monomeric Ruthenium Complex." Angeles-Boza, A. M.; Roth, J. P. *Inorg. Chem.* **2012**, *51*, 4722-4729.

(4) "Hydrogen Tunneling Steps in Cyclooxygenase-2 Catalysis." Danish, H. H.; Doncheva, I. S.; Roth, J. P. *J. Am. Chem. Soc.* **2011**, *133*, 15846-15849.

(5*) Huff, G. S.; Doncheva, I. S.; Brinkley, D. W.; Angeles-Boza, A. M.; Mukherjee, A.; Cramer, C. J.; Roth , J. P. "Experimental and Computational Investigations of Oxygen Reactivity in a Heme and Tyrosyl Radical-Containing Fatty Acid α-(Di)oxygenase." *Biochemistry* **2011**, *50*, 7375-7389.

(6) Mukherjee, A.; Angeles-Boza, A. M.; Huff, G. S.; Roth, J. P. "Catalytic Mechanism of a Heme and Tyrosyl Radical-Containing Fatty Acid α-(Di)oxygenase." *J. Am. Chem. Soc*. **2011**, *133*, 227-238.

(7*) "Oxygen Isotope Effects as Structural and Mechanistic Probes in Inorganic Oxidation Chemistry." Ashley, D. C.; Brinkley, D. W.; Roth, J. P. Inorg. Chem. Special Forum on O_2 Reduction **2010** 49, 3661-3675.

(8) Roth, J. P. "Oxygen Isotope Effects as Probes of Electron Transfer Mechanisms and Structures of Activated O_2." *Acc. Chem. Res.,* **2009**, 399-408

(9) Smirnov, V. V.; Lanci, M. P.; Roth, J. P. "Computational Modeling of Oxygen Isotope Effects on Metal-Mediated O_2 Activation at Varying Temperatures." *J. Phys. Chem. A* **2009**, *113,* 1934-1945.

(10) Roth, J. P.; C. J. Cramer "Direct Examination of H_2O_2 Activation by a Heme Peroxidase." *J. Am. Chem. Soc.* **2008**, *130*, 7802-7803.

VI. Potential Conflicts of Interest:

A. Collaborators and Co-Authors: Prof. Christopher J. Cramer, Prof. David M. Dooley, Prof. Richard Debus, Prof. Warwick Hillier, Prof. Donald J. Kurtz, Prof. Rajeev Pabhakar

B. Graduate Student and Post-Doc Adviser/Advisees:

1. Grad Student Advisor: Prof. James. M. Mayer
2. Post-Doc Advisor: Prof. Judith P. Klinman
3. List of Grads and Post-Doc with current affiliations: Dr. Michael P. Lanci (Exxon-Mobil), Dr. Arnab Mukherjee (Univ. Illinois Urbana-Champaign, JHU), Prof. Valeriy V. Smirnov (Univ. Montana), Prof. Alfredo Angeles-Boza (Univ. Connecticut), Dr. Grace Y. Stokes (Univ. Utah), Dr. Rupam Sarma (Univ. Kentucky)

1.

Appendix 2: Current and Pending Support

A. Current

National Science Foundation MCB0919898 09/01/09-08/3/14
"Enzymatic C–H Oxidation by Tyrosyl Radicals"
This grant supports studies of a plant-derived fatty acid α-dioxygenase as a model for the homologous cyclooxygenase enzymes in mammals, of great biomedical importance.
Role: P.I.
$525,000 total

U.S. Department of Energy DE-PS02-09ER09-01 12/15/09-12/14/13
"Isotopic Studies of O–O Bond Formation during Water Oxidation"
This grant supports experimental and computational investigations of water oxidation by structurally defined inorganic complexes.
Role: P.I.
$499,727 total

Australian Research Council (ARC) DP120100872 01/01/12-12/31/14
"*The Mechanism of Photosynthetic Water Oxidation*"
This grant supports studies of photosystem II using oxygen-18 isotope effects.
Role: Co-PI with W. Hillier (Dept. of Biology, Australian National University), R. J. Debus (Dept. of Biochemistry, University of California, Riverside)
$701,020 total (Limited funds for research materials, postdoctoral support and travel funds may be provided from this grant).

B. Pending

National Institutes of Health
Collaborative supplement to GM040388-22
Role: Co PI (PI: Prof. Donald Kurtz University of Texas, San Antonio)

Appendix 3: References

1. McEvoy, J. P.; Brudvig, G. W. Water-splitting chemistry of photosystem II. *Chem. Rev.* (2006), 106, 4455-4483.
2. (a) Wasielewski, M. R. Photoinduced electron transfer in supramolecular systems for artificial photosynthesis. *Chem. Rev.* (1992), 92, 435-61. (b) Bard, A. J.; Fox, M. A. Photosynthesis: Solar Splitting of Water to Hydrogen and Oxygen. *Acc. Ch. Res.* (1995), 28, 141-145. (c) Gust, D.; Moore, T. A.; Moore, A.L. Solar Fuels via Artificial Photosynthesis *Acc. Chem. Res.*(2009), 42, 1890-1898.
3. (a) Lewis, N. S.; Nocera, D. G. Powering the planet: Chemical challenges in solar energy utilization. *Proc. Nat. Acad. Sci. U.S.A.*, (2006), 103, 15729-15735.
   (b) Eisenberg, R.; Gray, H. B. Preface on Making Oxygen. *Inorg. Chem.* (2008), 47, 1697-1699.
4. Sarma, R.; Angeles-Boza, A. M.; Brinkley, D. W.; Roth, J. P. Studies of the Di-iron(VI) Intermediate in Ferrate-Dependent Oxygen Evolution from Water. *J. Am. Chem. Soc.* (2012), 134, 15371-15386.
5. Romain, S.; Vigara, L.; LLobet, A. Oxygen-Oxygen Bond Formation Pathways Promoted by Ruthenium Complexes. *Acc. Chem. Res.* (2009), 42, 1944-1953.
6. Roth, J. P.; Cramer, C. J. Direct Examination of H_2O_2 Activation by a Heme Peroxidase. *J. Am. Chem. Soc.* (2008), 130, 7802-7803.
7. Erbs, W.; Desilvestro, Borgarello, E.; Grätzel, M. Visible-Light O_2 Generation from Aqueous Dispersions of WO_3. *J. Phys. Chem.* (1984), 88, 4001-4006.
8. (a) Bigeleisen, J. *Isotope Effects in Chemistry and Biology*; Kohen, A., Limbach, H.H., Eds.; CRC Press: Boca Raton (2005) p. 1-39. (b) Wolfsberg, M. *Isotope Effects in Chemistry and Biology*; Kohen, A., Limbach, H.H., Eds.; CRC Press: Boca Raton (2005) p. 89-117. (c) Wolfsberg, M.; Van Hook, W. A.; Paneth, P. *Isotope Effects: In the Chemical, Geological, and Bio Sciences*, Springer, New York: 2010.
9. (a) Ashley, D. C.; Brinkley, D. W.; Roth, J. P. *Inorg. Chem*. (2010), 49, 3661. (b) Roth, J. P. in *Physical Inorganic Chemistry: Methods and Techniques* Vol. 1, Wiley, New York: 2010, p. 425. (c) Smirnov, V. V.; Brinkley, D. W.; Lanci, M. P.; Karlin, K. D. Roth, J. P. Probing Metal-Mediated O2 Activation in Chemical and Biological Systems. *J. Molec. Catal. A* (2006) 251, 100-107.
10. Guy, R. D.; Fogel, M. L.; Berry, J. A. Photosynthetic fractionation of the stable isotopes of oxygen and carbon. *Plant Physiol.* (1993), 101, 37-47.
11. Huskey, W. P. in *Enzyme Mechanism from Isotope Effects*, Ed. Cook, P. F. CRC Press, Boca Raton: 1991, p. 37.
12. (a) Angeles-Boza, A. M.; Roth, J. P. Oxygen Kinetic Isotope Effects upon Catalytic Water Oxidation by a Monomeric Ruthenium Complex. *Inorg. Chem.* (2012) 51, 4722-4729. (b) Angeles-Boza, A. M. Ertem, M. Z.; Sarma, R. Ibañez, C. H.; Maji, S.; Llobet, A.; Cramer, C. J. Roth, J. P. Oxygen-18 Kinetic Isotope Effects on Water Oxidation by Monomeric and Dimeric Ruthenium Catalysts. (2013) *submitted*.

13. (a) Goff, H.; Murmann, R. K. Mechanism of isotopic oxygen exchange and reduction of ferrate(VI) ion (FeO_4^{2-}). *J. Am. Chem. Soc.* (1971), 93, 6058-6065. (b) Wood, R. H. The Heat, Free Energy and Entropy of the Ferrate(VI) Ion. *J. Am. Chem. Soc.* (1958), 80, 2038-2041.
14. Liu, Y.; Mukherjee, A.; Nahumi, N.; Ozbil, M.; Brown, D.; Angeles-Boza, A. M.; Dooley, D. M.; Prabhakar, R.; Roth, J. P. Experimental and Computational Evidence of Metal-O_2 Activation and Rate-Limiting Proton-Coupled Electron Transfer in a Copper Amine Oxidase. *J. Phys. Chem. B* (2013), 117, 218-229.
15. (a) Smirnov, V. V.; Lanci, M. P.; Roth, J. P. Computational Modeling of Oxygen Isotope Effects on Metal-Mediated O_2 Activation at Varying Temperatures. J. Phys. Chem. A (2009), 113, 1934-1945. (b) Lanci, M. P.; Smirnov, V. V.; Cramer, C. J.; Gauchenova, E. V.; Sundermeyer, J.; Roth, J. P. Isotopic Probing of Molecular Oxygen Activation at Copper(I) Sites. *J. Am. Chem. Soc.* (2007), 129, 14697-14709.
16. (a) Perdew, J. P. Unified Theory of Exchange and Correlation Beyond the Local Density Approximation In Electronic Structure of Solids '91; Ziesche, P., Eschrig, H., Eds.; Akademie Verlag: Berlin, 1991, pp. 11-20. (b) Adamo, C.; Barone, V. Exchange functionals with improved long-range behavior and adiabatic connection methods without adjustable parameters: The mPW and mPW1PW models. *J. Chem. Phys.* (1998), 108, 664-675.
17. C. J. Cramer, Essentials of Computational Chemistry: Theories and Models; 2nd ed.; John Wiley & Sons: Chichester, 2004.
18. (a) Clausen, J.; Junge, W. Detection of an intermediate of photosynthetic water oxidation. *Nature* (2004), 430, 480-483.
19. Haumann, M.; Liebisch, P.; Mueller, C.; Barra, M.; Grabolle, M.; Dau, H. Photosynthetic O_2 Formation Tracked by Time-Resolved X-ray Experiments. *Science* (2005), 310, 1019-1021.
20. (a) Tcherkez, G.; Farquhar, G. D. On the ^{16}O:^{18}O isotope effect associated with photosynthetic O_2 production. *Functional Plant Biology* (2007), 34, 1049-1052. (b) Burda, K.; Bader, K. P.; Schmid, G. H. ^{18}O isotope effect in the photosynthetic water splitting process. *Biochim. Biophys. Acta, Bioenerg*. (2003), 1557, 77-82. (c) Metzner, H.; Fischer, K.; Bazlen, O. Isotope ratios in photosynthetic oxygen. *Biochim. Biophys. Acta, Bioenerg*. (1979), 548, 287-95.
21. (a) Wasylenko, D. J.; Ganesamoorthy, C.; Koivisto, B. D.; Henderson, M. A.; Osthoff, H. D.; Berlinguette, C. P. Electronic Modification of the $[RuII(tpy)(bpy)(OH_2)]^{2+}$ Scaffold: Effects on Catalytic Water Oxidation. *J. Am. Chem. Soc.* (2010), 132, 16094-16106. (b) Masaoka, S.; Sakai, K. Clear Evidence Showing the Robustness of a Highly Active Oxygen-evolving Mononuclear Ruthenium Complex with an Aqua Ligand. *Chem. Lett.* (2009), 38, 182-183. (c) Wasylenko, D. J.; Ganesamoorthy, C.; Henderson, M. A.; Berlinguette, C. P. Unraveling the Roles of the Acid Medium, Experimental Probes, and Terminal Oxidant, $(NH_4)_2[Ce(NO_3)_6]$, in the Study of a Homogeneous Water Oxidation Catalyst. *Inorg. Chem.* (2011), 50, 3662-3672. (d) Wasylenko D. J.; Ganesamoorthy, C.;

Koivisto, B. D.; Henderson, M. A.; Berlinguette, C. P. Insight into Water Oxidation by Mononuclear Polypyridyl Ru Catalysts. *Inorg. Chem.* (2010), 29, 2202-2209.

22 . (a) Cape, J. L.; Siems, W. F.; Hurst, J. K.; Cape, J.L.; Lymar, S. V.; Lightbody, T.; Hurst, J.K. Pathways of Water Oxidation Catalyzed by Ruthenium “Blue Dimers” Characterized by ^{18}O-Isotopic Labeling. *Inorg. Chem.* (2009), 48, 8729-8735. (b) Hamada, H.; Siems, W. F.; Koike, T.; Hurst, J.K. Mechanisms of Water Oxidation Catalyzed by the cis,cis-$[(bpy)_2Ru(OH_2)]_2O^{4+}$ Ion. *J. Am. Chem. Soc.* (2004), 126, 9786-9795. (c) Binstead, R.A.; Chronister, C. W.; Ni, J.; Hartshorn, C. M.; Meyer, T. J. Mechanism of Water Oxidation by the μ-Oxo Dimer $[(bpy)_2(H_2O)Ru^{III}ORu^{III}(OH_2)(bpy)_2]^{4+}$. *J. Am. Chem. Soc.* (2000), 122, 8464-8473. (d) Geselowitz, D. A.; Meyer, T.J. Water oxidation by μ-oxobis [bis(bipyridine)oxoruthenium(V)](4+). An oxygen-labeling study. *Inorg. Chem.* (1990), 29, 3894-3896.

23 . (a) Sens, C.; Romero, I.; Rodriguez, M.; Llobet, A.; Parella, T.; Benet-Buchholz, J. A New Ru Complex Capable of Catalytically Oxidizing Water to Molecular Dioxygen. *J. Am. Chem. Soc.* (2004), 126, 7798-7799. (b) Romain, S.; Bozoglian, F.; Sala, X.; Llobet, A. Oxygen−Oxygen Bond Formation by the Ru-Hbpp Water Oxidation Catalyst Occurs Solely via an Intramolecular Reaction Pathway. *J. Am. Chem. Soc.* (2009), 131, 2768-2769. (c) Bozoglian, F.; Romain, S. Ertem, M. Z.; Todorova, T. K.; Sens, C.; Mola, J.; Rodrıguez, M.; Romero, I.; Benet-Buchholz, J. ; Fontrodona, X.; Cramer, C. J.; Gagliardi, L.; Llobet, A. The Ru−Hbpp Water Oxidation Catalyst. *J. Am. Chem. Soc.* (2009), 131, 15176-15187.

24. (a) Moonshiram, D.; Purohit, V.; Concepcion, J. J.; Meyer, T. J.; Pushkar, Y. Mechanism of Catalytic Water Oxidation by the Ruthenium Blue Dimer Catalyst: Comparative Study in D_2O versus H_2O (2013) *Materials*, 6, 392. (b) Chen, Z.; Concepcion, J. J.; Hu, Q.; Yang, W.; Hoertz, P. G.; Meyer, T. J. . Concerted O atom–proton transfer in the O—O bond forming step in water oxidation.*Proc. Natl. Acad. Sci. USA.* 2010, **107**, 7225.

25. Combustion was carried out by recirculation over Pt/graphite furnace ca. 850 °C while the pressure of O_2 was monitored.

26. Rutenburg, A. C.; Taube, H. The Exchange of Water between $Co(NH_3)_5H2O^{+++}$ and Solvent. *J. Chem. Phys*. (1952), 20, 825-826. (b) Friedman, H. L.; Taube, H.; Hunt, J. P. Photolysis of Methyl Iodide. *J. Chem. Phys.* (1950), 18, 760.

27. (a) Guarr, T.; Buhks, E.; McLendon, G. Quantum effects of high-frequency modes in inorganic electron transfer: kinetic isotope effects in redox reactions of hexaaquairon(2+) ion ($[Fe(H_2O)_6]2+$, hexa(aqua-d2)iron(2+) ion ($[Fe(D_2O)_6]2+$), and hexa(aqua-18O)iron(2+) ion ($[Fe(^{18}OH_2)_6]2+$). *J. Am. Chem. Soc.* (1983), 105, 3763-3767. (b) Buhks, E.; Bixon, M.; Jortner, J. Deuterium isotope effects on outer-sphere electron-transfer reactions. *J. Phys. Chem.* (1981), 85, 3763-3766.

28. Huff, G. S.; Doncheva, I. S.; Brinkley, D. W.; Angeles-Boza, A. M.; Mukherjee, A.; Cramer, C. J.; Roth, J. P. Experimental and Computational Investigations of Oxygen Reactivity in a Heme and Tyrosyl Radical-Containing Fatty Acid α-(Di)oxygenase. *Biochemistry.* (2011), 50, 7375-7389.

29. (a) Lanci, M. P.; Brinkley, D. W.; Stone, K. L.; Smirnov, V. V.; Roth, J. P. Structures of

Transition States in Metal-Mediated O_2 Activation Reactions. *Angew. Chem. In. Ed.* 2005, *44*, 7273-7276. (b) Lanci, M. P.; Roth, J. P. Oxygen Isotope Effects upon Reversible O_2-Binding Reactions: Characterizing Mononuclear Superoxo and Peroxo Structures. *J. Am. Chem. Soc.* (2006), 128, 16006-16007. (c) Roth, J. P. Oxygen Isotope Effects as Probes of Electron Transfer Mechanisms and Structures of Activated O_2. *Acc. Chem. Res.,* (2009), 399-408.

30. Non-analytic integral evaluations made use of a pruned grid having 99 radial shells and 590 angular points per shell. An automatically generated density-fitting basis set was used within the resolution-of-the-identity approximation to speed the evaluation of Coulomb integrals.
31. Perdew, J. P. "Unified Theory of Exchange and Correlation Beyond the Local Density Approximation" In Electronic Structure of Solids '91; Ziesche, P., Eschrig, H., Eds.; Akademie Verlag: Berlin, 1991, pp. 11-20; Adamo, C.; Barone, V. *J. Chem. Phys.* (1998) 108, 664-675.
32. (a) Hay, P. J.; Wadt, W. R. Ab initio effective core potentials for molecular calculations. Potentials for the transition metal atoms Sc to Hg. *J. Chem. Phys.* (1985), 82, 270-283; (b) Hay, P. J.; Wadt, W. R. Ab initio effective core potentials for molecular calculations. Potentials for main group elements Na to Bi. *J. Chem. Phys.* (1985), 82, 284-298; Hay, P. J.; Wadt, W. R. Ab initio effective core potentials for molecular calculations. Potentials for K to Au including the outermost core orbitals. *J. Chem. Phys.* (1985), 82, 299-311.
33. Calculations were carried out using the Gaussian09 package.
34. (a) Zhao, Y.; Truhlar, D. G. A new local density functional for main-group thermochemistry, transition metal bonding, thermochemical kinetics, and noncovalent interactions. *J. Chem. Phys.* (2006), 125, 194101-194119. (b) Zhao, Y.; Truhlar, D. G. Density Functionals with Broad Applicability in Chemistry. *Acc. Chem. Res.* (2008), 41, 157-167. (c) Zhao, Y.; Truhlar, D. G. The M06 suite of density functionals for main group thermochemistry, thermochemical kinetics, noncovalent interactions, excited states, and transition elements: two new functionals and systematic testing of four M06-class functionals and 12 other functionals. *Theor. Chem. Acc.* (2008), 215-241.
35. Andrae, D.; Haeussermann, U.; Dolg, M.; Stoll, H.; Preuss, H. Energy-adjusted *ab initio* pseudopotentials for the second and third row transition elements. *Theor. Chim. Acta.* (1990), 77, 123-141.
36. Hehre, W. J.; Radom, L.; Schleyer, P. V. R. ; Pople, J. A. Ab Initio Molecular Orbital Theory; Wiley: New York, 1986.
37. Cramer, C. J. ; Essentials of Computational Chemistry: Theories and Models; 2nd ed.; John Wiley & Sons: Chichester, 2004.
38. Marenich, A. V.; Cramer, C. J.; Truhlar, D. G. Universal Solvation Model Based on Solute Electron Density and on a Continuum Model of the Solvent Defined by the Bulk Dielectric Constant and Atomic Surface Tensions. *J. Phys. Chem. B* (2009), 113, 6378-6396.
39. (a) Ziegler, T.; Rauk, A.; Baerends, E. J. On the calculation of multiplet energies by the hartree-fock-slater method. *Theor. Chim. Acta*. (1977), 43, 261-271. (b) Noodleman, L.

Valence bond description of antiferromagnetic coupling in transition metal dimers. *J. Chem. Phys.* (1981), 74, 5737-5744. (c) Cramer, C. J.; Truhlar, D. G. Density functional theory for transition metals and transition metal chemistry. *Phys. Chem. Chem. Phys.* (2009), 11, 10757-10816.

40. (a) Yamaguchi, K.; Jensen, F. ; Dorigo, A.; Houk, K. N. A spin correction procedure for unrestricted Hartree-Fock and Møller-Plesset wavefunctions for singlet diradicals and polyradicals. *Chem. Phys. Lett.* (1988), 149, 537-542. (b) Soda, T. ; Kitagawa, Y.; Onishi, T.; Takano, Y.; Shigeta, Y.; Nagao, H.; Yoshioka, Y. Yamaguchi, K. Ab initio computations of effective exchange integrals for H–H, H–He–H and Mn_2O_2 complex: comparison of broken-symmetry approaches. *Chem. Phys. Lett.* (2000), 319, 223-230.
41. (a) Noodleman, L.; Peng, C. Y.; Case, D. A.; Mouesca, J.-M. Orbital interactions, electron delocalization and spin coupling in iron-sulfur clusters. *Coord. Chem. Rev.* (1995), 144, 199-244. (b) Ciofini, I.; Daul, C. A. DFT calculations of molecular magnetic properties of coordination compounds. *Coord. Chem. Rev.* (2003), 238, 187-209. (c) Harvey, J. N. DFT Computation of Relative Spin-State Energetics of Transition Metal Compounds. *Struct. Bond.* (2004), 112, 151-184. (d) Neese, F. Prediction of molecular properties and molecular spectroscopy with density functional theory: From fundamental theory to exchange-coupling. *Coord. Chem. Rev.* (2009), 253, 526-563.
42. Hughes, T. F.; Friesner, R. A. Systematic Investigation of the Catalytic Cycle of a Single Site Ruthenium Oxygen Evolving Complex Using Density Functional Theory. *J. Phys. Chem B.* (2011), 115, 9280-9289.
43. Bianco, R.; Hay, P. J.; Hynes, J. T. Theoretical Study of O–O Single Bond Formation in the Oxidation of Water by the Ruthenium Blue Dimer. *J. Phys. Chem. A* (2011), 115, 8003-8016.
44. Weaver, T. R.; Meyer, T. J.; Adeyemi, S. A.; Brown, G. M.; Eckberg, R. P.; Hatfield, W. E.; Johnson, E. C.; Murray, R. W.; Untereker, D. Chemically significant interactions between ruthenium ions in oxo-bridged complexes of ruthenium(III). *J. Am. Chem. Soc.* 1975, **97**, 3039.
45. (a) Moonshiram, D.; Jurss, J. W.; Concepcion, J. J.; Zakharova, T.; Alperovich, I.; Meyer, T. J.; Pushkar, Y. Structure and Electronic Configurations of the Intermediates of Water Oxidation in Blue Ruthenium Dimer Catalysis. *J. Am. Chem. Soc.* 2012, **134**, 4625. (b) Stull, J. A.; Stich, T. A.; Hurst, J. K.; Britt, R. D. Electron Paramagnetic Resonance Analysis of a Transient Species Formed During Water Oxidation Catalyzed by the Complex Ion [(bpy)2Ru(OH2)]2O4+. *Inorg. Chem.* 2013, **52**, 4578. (c) Cape, J.L.; Lymar, S. V.; Lightbody, T.; Hurst, J.K. . Characterization of Intermediary Redox States of the Water Oxidation Catalyst, [Ru(bpy)(OH2)]2O4+. *Inorg. Chem.* 2009, **48**, 4400.
46. Yang, X.; Baik, M. H. Cis,cis-[(bpy)2RuVO]2O4+ Catalyzes Water Oxidation Formally via in Situ Generation of Radicaloid RuIV−O•. *J. Am. Chem. Soc.* 2006, **128**, 7476.
47. Blakemore, J. D.; Schley, N. D.; Balcells, D.; Hull, J. F.; Olack, G. W.; Incarvito, C. D.; Eisenstein, O.; Brudvig, G. W.; Crabtree, R. H. Half-sandwich iridium complexes for homogeneous water oxidation catalysis *J. Am. Chem. Soc.* (2010), 132, 16017-16029.

48. Curtin, P. N.; Tinker, L. L.; Burgess, C. M.; Cline, E. D.; Bernhard, S. Structure-activity correlations among iridium(III) photosensitizers in a robust water-reducing system *Inorg. Chem.* (2009), 48, 10498-10506.
49. Sarma, R. Angeles-Boza, A. M. Roth, J. P. Oxygen isotope effects expose the O-O bond forming step in catalysis by an aqueous soluble and robust organometallic iridium complex. In preparation.
50. Barnett, S. M.; Goldberg, K. I.; Mayer, J. M. A soluble copper-bipyridine water-oxidation electrocatalyst. *Nature Chemistry* (2012), 4, 498-502.
51. Anbar, M.; Taube, H. Oxygen isotope effects at anodes. *J. Am. Chem. Soc.* (1956), 78, 3252-3255.
52. Schley, N. D.; Blakemore, J. D.; Subbaiyan, N. K.; Incarvito, C. D.; D'Souza, F.; Crabtree, R. H.; Brudvig, G. W. Distinguishing Homogeneous from Heterogeneous Catalysis in Electrode-Driven Water Oxidation with Molecular Iridium Complexes. *J. Am. Chem. Soc.* (2011), 133, 10473-10481.
53. Kushner-Lenhoff, M. N.; Blakemore, J. D.; Schley, N. D.; Crabtree, R. H.; Brudvig, G. W. Effects of aqueous buffers on electrocatalytic water oxidation with an iridium oxide material electrodeposited in thin layers from an organometallic precursor. *Dalton Trans.* (2013), 42, 3617-3622.
54. Blakemore, J. D.; Schley, N. D.; Kushner-Lenhoff, M. N.; Winter, A. M.; D'Souza, F.; Crabtree, R. H.; Brudvig, G. W. Comparison of Amorphous Iridium Water-Oxidation Electrocatalysts Prepared from Soluble Precursors. *Inorg. Chem.* (2012), 51, 7749-7763.
55. (a) Limburg, J.; Vrettos, J. S.; Liable-Sands, L. M.; Rheingold, A. L.; Crabtree, R. H.; Brudvig, G. W. A functional model for O-O bond formation by the O_2-evolving complex in photosystem II. *Science* (1999), 283, 1524-1527. (b) Limburg, J.; Szalai, V. A.; Brudvig, G. W. A mechanistic and structural model for the formation and reactivity of a $Mn^{V}O$ species in photosynthetic water oxidation. J. Chem. Soc., Dalton Trans. (1999), 9, 1353-1362.
56. (a) Tagore, R.; Chen, H.; Zhang, H.; Crabtree, R.H.; Brudvig, G. W. Homogeneous water oxidation by a di-μ-oxo dimanganese complex in the presence of Ce^{4+}. *Inorg. Chim. Acta.* (2007), 360, 2983-2989. (b) Gao, Y.; Crabtree, R. H.; Brudvig, G.W. Water Oxidation Catalyzed by the Tetranuclear Mn Complex $[Mn(IV)_4O_5(tpy)_4(H_2O)_2](ClO_4)_6$. *Inorg. Chem.* (2012), 51, 4043-4050.
57. Lundberg, M.; Blomberg, M. R. A.; Siegbahn, P. E. M. Oxyl radical required for O-O bond formation in synthetic Mn-catalyst. *Inorg. Chem.* (2004), 43, 264-274.
58. Fillol, J. L.; Codola, Z.; Garcia-Bosch, I.; Gomez, L.; Pla, J. J.; Costas, M. Efficient water oxidation catalysts based on readily available iron coordination complexes. *Nature Chemistry* (2011), 3, 807-813.
59. (a) Lim, M. H.; Rohde, J-U; Stubna, A.; Bukowski, M. R.; Costas, M.; Ho, R. Y. N.; Munck, E.; Nam, W.; Que, L, Jr. An FeIV=O complex of a tetradentate tripodal nonheme ligand. *Proc. Nat. Acad. Sci. USA* (2003), 100, 3665-3670. (b) Paine, T. K.; Costas, M.; Kaizer, J.; Que, L., Jr. Oxoiron(IV) complexes of the tris(2-pyridylmethyl)amine ligand family: effect of pyridine α-substituents. *J. Biol. Inorg. Chem*. (2006), 11, 272-276.

60. Smirnov, V. V.; Roth, J. P. Evidence for CuO_2 Intermediates in Superoxide Oxidations by Biomimetic Copper(II) Complexes. *J. Am. Chem. Soc.* (2006) 128, 3683-3695.
61. Ertem, M.Z.; Gagliardi, L.; Cramer, C. J. Quantum chemical characterization of the mechanism of an iron-based water oxidation catalyst. *Chem. Science* (2012) 3, 1293-1299.
62 . Wang, H.; Deutsch, T.; Turner, J. A. A. Direct water splitting under visible light with a nanostructured photoanode and $GaInP_2$ photocathode. *Electrochem.Soc. Transactions* (2008) 6, 37-44.
63. Waller, M. R.; Townsend, T. K. Zhao, J.; Sabio, E. M.; Chamousis, R. L.; Browning, N. D.; Osterloh, F. E. Single crystal tungsten oxide nanosheets: Photochemical water oxidation in the quantum confinement regime. *Chemistry of Materials* (2012) 24, 698-704.
64. (a) Biswas, S. K.; Baeg, J-O. A facile one-step synthesis of single crystalline hierarchical WO_3 with enhanced activity for photo-electrochemical solar water oxidation. *Int. J. Hydrogen Energy* (2013) 38, 3177-3188. (b) Ramana, C. V.; Utsunomiya, S.; Ewing, R. C.; Julien, C. M.; Becker, U. Structural stability and phase transitions in WO_3 thin films. *J. Phys. Chem. B* 2006, *110,* 10430-10435